INL/RPT-23-74691
Revision 0

Molten Salt Tritium Transport Experiment

September 2023

A Versatile Fluoride Salt Loop for Validation of Tritium Transport Phenomena

Thomas F. Fuerst, Chase N. Taylor, Adriaan A. Riet, and Joseph R. Redmond
Irradiated Fuels and Materials Department, Idaho National Laboratory

Subash Sharma and Anthony Bowers
Chemical Engineering Department, University of Massachusetts Lowell

Travis Mui, Yifan Mao, and Rui Hu
Argonne National Laboratory

Idaho National Laboratory

INL is a U.S. Department of Energy National Laboratory operated by Battelle Energy Alliance, LLC

DISCLAIMER

This information was prepared as an account of work sponsored by an agency of the U.S. Government. Neither the U.S. Government nor any agency thereof, nor any of their employees, makes any warranty, expressed or implied, or assumes any legal liability or responsibility for the accuracy, completeness, or usefulness, of any information, apparatus, product, or process disclosed, or represents that its use would not infringe privately owned rights. References herein to any specific commercial product, process, or service by trade name, trade mark, manufacturer, or otherwise, does not necessarily constitute or imply its endorsement, recommendation, or favoring by the U.S. Government or any agency thereof. The views and opinions of authors expressed herein do not necessarily state or reflect those of the U.S. Government or any agency thereof.

INL/RPT-23-74691

Molten Salt Tritium Transport Experiment

A Versatile Fluoride Salt Loop for Validation of Tritium Transport Phenomena

Thomas F. Fuerst, Chase N. Taylor, Adriaan A. Riet, and Joseph R. Redmond
Irradiated Fuels and Materials Department, Idaho National Laboratory

Subash Sharma and Anthony Bowers
Department of Chemical Engineering, University of Massachusetts Lowell

Travis Mui, Yifan Mao, and Rui Hu
Argonne National Laboratory

September 2023

Idaho National Laboratory
Idaho Falls, Idaho 83415

http://www.inl.gov

Prepared for the
U.S. Department of Energy
Office of Nuclear Energy
Under DOE Idaho Operations Office
Contract DE-AC07-05ID14517

Page intentionally left blank

INL ART Program

Molten Salt Tritium Transport Experiment

INL/RPT-23-74691
Revision 0

September 2023

Technical Reviewer: (Confirmation of mathematical accuracy, and correctness of data and appropriateness of assumptions.)

	09/27/2023
Hanns Gietl Research Scientist	Date

Approved by:

	9/28/2023
Michael E. Davenport ART Project Manager	Date
	9/27/2023
Michelle T. Sharp INL Quality Assurance	Date

ABSTRACT

Tritium is generated in Molten Salt Reactors (MSRs) from neutron capture by lithium and other constituents of the molten salt FLiBe. Tritium is a unique radionuclide as it readily permeates through hot structural materials. Thus, any material in contact with tritium-laden molten salt is a potential pathway for release. Understanding tritium transport and devising adequate control strategies are necessary for the safe operation of MSRs. The Molten Salt Tritium Transport Experiment (MSTTE) is a forced-convection fluoride salt loop with the capability to inject hydrogen isotopes into flowing molten salt and to measure transport phenomena such as permeation through metals and evolution from free-surfaces. MSTTE is designed to be versatile to test potential control technology in future campaigns. This report focuses on the current design and analysis of MSTTE. Custom designed and fabricated experiment components such as the hydrogen injection system, permeation test section, diagnostics, and gas distribution system are discussed in detail. System-level tritium transport modeling using the System Analysis Module investigates experiment parameters such as hydrogen source terms, salt flow rate, and salt temperature. Computational fluid dynamics (CFD) of the salt flow in the permeation test section informs design choices to establish fully developed flow in the measured permeation zone.

Page intentionally left blank

CONTENTS

1. BACKGROUND 1
1.1 Tritium Generation 1
1.2 Tritium Transport 5
2. MOLTEN SALT TRITIUM TRANSPORT EXPERIMENT DESIGN 6
2.1 Components 8
2.1.1 Copenhagen Atomics Pumped Portable Salt Loop 8
2.1.2 Hydrogen Injection System 9
2.1.3 Permeation Test Section and Vacuum Diagnostics 11
2.1.4 Plenum 13
2.1.5 Gas Distribution System 13
2.2 External Test Section Pressure Drop 14
2.3 Stress Analysis 18
2.3.1 Loop Stress Analysis 18
2.3.2 Support Stress Analysis 19
3. MSTTE TRITIUM TRANSPORT ANALYSIS 21
3.1 Tritium Transport Model in SAM 21
3.2 Verification with an Analytical Permeator Model 22
3.3 SAM Model of MSTTE 23
3.4 Parametric Study of Predicted Permeation Rates 25
4. MSTTE TEST SECTION CFD 27
4.1 Turbulence Modeling 27
4.2 Overview of CFD Results 29
4.3 Analysis of Reducers 31
4.3.1 Concentric Reducer/Expander CFD Results 32
4.3.2 Eccentric Reducer/Expander CFD Results 34
4.3.3 Reversed Eccentric Reducer/Expander 36
4.4 Analysis of Flow Conditioners 38
4.5 CFD Future Work 43
5. SUMMARY 44
6. REFERENCES 45
Appendix A Numerical Model for Hydrogen Transport 47
Appendix B Code Compliance Calculations 49
Appendix C Additional Information on CFD Analysis 51

FIGURES

Figure 1. Environmental pathways considered for tritium dose calculations [7]. 2

Figure 2. Activation and decay schemes of lithium and beryllium associated with tritium [13]. 4

Figure 3. Neutron absorption cross section of nuclides relevant to tritium generation in molten salts [14]. 4

Figure 4. Computer Aided Design (CAD) rendering of MSTTE. The worker in the drawing is 6 ft for reference. 7

Figure 5. Cross section of MSTTE with major components listed. 7

Figure 6. Pumped salt loop from Copenhagen Atomics [17]. 8

Figure 7. Front (a) and back (b) of as-built Copenhagen Atomics Salt Loop for MSTTE at the Copenhagen Atomics facility. 9

Figure 8. (a) Original HIS with five-tube design and (b) updated HIS including three-tube design. 10

Figure 9. Section view of the HIS. 10

Figure 10. Permeation calculations for both five-(original) and three-(updated) tube designs. 11

Figure 11. Permeation test section, length scales, and diagnostics. 12

Figure 12. Analytical solution for permeated hydrogen flow rate through test section with varying experimental variables. 12

Figure 13. CAD of MSTTE plenum. 13

Figure 14. Piping and Instrumentation Diagram (P&ID) for MSTTE. 14

Figure 15. External test section with components labeled. 17

Figure 16. Pressure drops through the external test section for FLiNaK and FLiBe as a function of salt flow rate at 600°C. 17

Figure 17. Modeled von Mises stress of the MSTTE loop at 700°C. 18

Figure 18. Side mounting geometry. 19

Figure 19. Mesh geometry of side mounting geometry. 19

Figure 20. Example of braced rod configuration. 20

Figure 21. Unbraced (top) and braced (bottom) rod displacement, stress, and temperature. 20

Figure 22. Comparison of normalized tritium concentrations in the fluid bulk region (left), in the fluid near the wall (center), and in the solid at the wall surface (right) as predicted by SAM versus the analytically derived concentration profiles [31]. 23

Figure 23. SAM model of the MSTTE facility with predicted fluid pressure distributions (Pa) at nominal conditions with profile (left) and skewed (right) point of views. 24

Figure 24. Tritium permeation rates through the test section outer wall (left) and the average T_2 concentrations in the test section (right) under nominal flow at different injection rates. 25

Figure 25. Tritium permeation rates through the test section outer wall for different flow rates at 600°C temperature (left) and for different temperatures at 100 LPM flow (right). 26

Figure 26. Average T_2 concentrations in the test section for different flow rates at 600°C temperature (left) and for different temperatures at 100 LPM flow (right). 26

Figure 27. Entrance length versus salt flow rate for FLiNaK and FLiBe at 600 °C using current design specifications. 27

Figure 28. Mesh grid for top and bottom bend of MSTTE external test section (left). Mesh grid for the permeator test section (right). 29

Figure 29. Normalized velocity vector field for 10 LPM (top) and 100 LPM (bottom). 30

Figure 30. Streamlines visualizing the swirling effect caused by the flow separation in the 85° bend. 30

Figure 31. Velocity profiles for turbulent 100 LPM case. 31

Figure 32. Geometrical representation of the concentric (top) and eccentric (bottom) reducers. 31

Figure 33. Eccentric (top) and reversed eccentric (bottom) reducer geometries. 32

Figure 34. Mesh used for concentric (left) and eccentric (right) reducers. 32

Figure 35. Velocity profiles at the test section vacuum boundary entrance for the 1 inch concentric reducers. 33

Figure 36. Velocity profiles at the test section vacuum boundary entrance for the 0.5 inch concentric reducers. 33

Figure 37. The location identification for the 0.5 in. concentric reducers velocity profiles (left); velocity profiles in the XZ-Plane (top-right) and XY-Plane (bottom-right). 34

Figure 38. Velocity profile at the test section vacuum boundary entrance for 1-in. concentric reducer. 35

Figure 39. Velocity profile at the test section vacuum boundary entrance for 0.5-in. eccentric reducer. 35

Figure 40. The location identification for the 0.5-in eccentric reducers velocity profiles (left); velocity profiles in the XZ-Plane (top-right) and XY-Plane (bottom-right). 36

Figure 41. Velocity profiles at the test section vacuum boundary entrance for 1 inch reversed eccentric reducer. 37

Figure 42. Velocity profiles at the test section vacuum boundary entrance for 0.5 inch reversed eccentric reducer. 37

Figure 43. The location identification for the 0.5 inch reversed eccentric reducers velocity profiles (left); velocity profiles in the XZ-Plane (top-right) and XY-Plane (bottom-right). 38

Figure 44. Laws flow conditioner design. 39

Figure 45. NEL flow conditioner design. 39

Figure 46. Streamlines with Laws type flow conditioner (top) and without conditioner (bottom). 40

Figure 47. The location identification for the Laws design flow conditioner (left); velocity profiles in the XZ-Plane (top-right) and XY-Plane (bottom-right). 41

Figure 48. The location identification for the NEL design flow conditioner (left); velocity profiles in the XZ-Plane (top-right) and XY-Plane (bottom-right). 42

Figure 49. Laws flow conditioner geometry with finite element evaluation of stress. 43

Figure B-1. Geometry definitions for Table B-3. 50

Figure C-1. MSTTE Permeator ANSYS geometry with dimensions. 52

TABLES

Table 1. Estimated tritium production rates (Ci GWe^{-1} y^{-1}) in various reactor types. 3

Table 2. Design Parameter Changes for the HIS. 9

Table 3. Fluid flow parameters for 100 LPM and loss coefficients for components. 14

Table 4. Pressure loss through components with 100 LPM salt flow rate at 600°C. 15

Table 5. Brace model summary. 20

Table 6. Species material properties included in SAM's built-in library that are used in the MSTTE facility model. 22

Table 7. SAM model parameters for a proposed FliBe-nickel permeator extractor [31]. 23

Table 8. MSTTE facility SAM model parameters and operating/boundary conditions. 23

Table 9. Predicted mass transfer coefficients, permeability, and average extraction efficiency ($[T_{2,in} - T_{2,out}] / T_{2,in}$) of the MSTTE test section under different flow conditions. 26

Table 10. Geometrical and physical properties of fluid and MSTTE permeator, respectively. 29

Table B-1. Straight pipe and bend equations and parameters. 49

Table B-2. Pipe thickness. 49

Table B-3. Branch reinforcement equations. 50

Table B-4. Branch reinforcement requirements. 50

Table C-1. Mesh information and metrics. 51

Page intentionally left blank

ACRONYMS

ALARA	as low as reasonably achievable
BC	boundary condition
BWR	boiling water reactors
CAD	computer aided design
CF	Conflat® flange
CFD	Computational fluid dynamics
DOE	U.S. Department of Energy
EPA	Environmental Protection Agency
FC	flow conditioner
FHR	fluoride salt-cooled high-temperature reactor
FY	fiscal year
HIS	hydrogen injection system
HTGR	high temperature gas cooled reactor
HTO	tritiated water
HWR	heavy water reactor
ID	inner diameter
INL	Idaho National Laboratory
IR	infrared
LIBS	laser induced breakdown spectroscopy
LPM	liters per minute
LWR	light water reactors
MSBR	molten salt breeder reactor
MSR	molten salt reactor
MSTDB	molten salt thermal properties database
MSTTE	molten salt tritium transport experiment
MTC	mass transfer coefficient
NRC	Nuclear Regulatory Commission
NRTL	Nationally Recognized Testing Laboratory
OBT	organically bound tritium
OD	outer diameter
PWR	pressurized water reactor
QMS	quadrupole mass spectrometers
SAM	system analysis module
STAR	safety and tritium applied research
SS	stainless steel

Page intentionally left blank

Molten Salt Tritium Transport Experiment

1. BACKGROUND

Molten salt reactors (MRSs) are a class of advanced nuclear fission reactor with a molten salt as the primary coolant. MSRs can be divided into subclasses by the phase of the fuel. The solid fuel subclass is typically referred to as a Fluoride salt-cooled High-temperature Reactor (FHR) and uses solid fuel particles with molten salt as the primary coolant [1]. The liquid fuel subclass has fissile material dissolved in the primary coolant salt, referred to as the fuel salt, and has a secondary coolant salt free of fuel.

Liquid-fueled MSRs have the capability of operating with the ^{233}U-^{232}Th fuel cycle. ^{232}Th is three times as abundant as uranium, has less weapons proliferation concern, less nuclear waste, and does not require fuel enrichment. However, ^{232}Th is fertile, thus it does not contain fissile isotopes such as ^{235}U, and requires fissile material from the uranium cycle for start-up. MSRs have the additional benefits of continuous fission-product removal and fuel processing, higher fuel burn-up, and high thermal efficiencies. Liquid-fueled reactors also have passive safety features such as a high coefficient of thermal expansion which results in a negative temperature coefficient of reactivity, low pressure operation, and no potential for steam explosion due to lack of water cooling. In accident scenarios, the fuel salt can be drained into criticality safe storage tanks [2].

While MSRs have many promising attributes, several technical issues remain. Corrosion of structural materials with molten salts remains a challenge. An ingress of moisture or oxide impurities can increase the redox potential and lead to higher corrosion rates [3-5]. The thermophysical properties of various fuel-salt mixtures remain uncertain and warrant the development of robust measurement programs and databases such as the Molten Salt Thermal Properties Database (MSTDB). Tritium production and mobility in MSRs remains a key challenge. Tritium is the only radionuclide that has potential for significant release under normal operating conditions due to its ability to diffuse through structural metals at an MSR's operational temperature (melting point of FLiBe is 459°C) [6]. Tritium production is unique to the molten salt $2LiF\text{-}BeF_2$ or Li_2BeF_4, referred to as FLiBe, where tritium is produced primarily though neutron capture of Li isotopes. However, FLiBe is the focus of many MSR concepts because it has excellent neutron moderation and thermal-hydraulic properties, it is optically transparent, and it does not react violently with water or air. Robust understanding of tritium transport phenomena and development of control technology is essential to the safe operation of future molten salt reactors using Li-containing salts.

1.1 Tritium Generation

Tritium (^3H) is the radioactive isotope of hydrogen that decays to ^3He releasing a low-energy beta particle with a half-life of 12.3 years. Elemental tritium gas (HT or T_2) is relatively benign due to its short biological half-life and weak absorption in the body. As an isotope of hydrogen, tritium reacts with oxygen to form tritiated water (HTO) as well as with organics to form organically bound tritium (OBT), which results in higher doses due to absorption in the body. For example, HTO has a biological half-life of 10 days and OBT has a biological half-life of 40 days. Gaseous HT can undergo beta-induced self-radiolysis with oxygen or water to form HTO, react on metal surfaces to form HTO, and convert to HTO through microorganisms in soil. Thus, tritium readily enters the atmosphere as water vapor and enters the hydrological cycle which affects drinking water as well as consumption of products like locally farmed plants and animals. The environmental pathways for tritium release are illustrated in Figure 1.

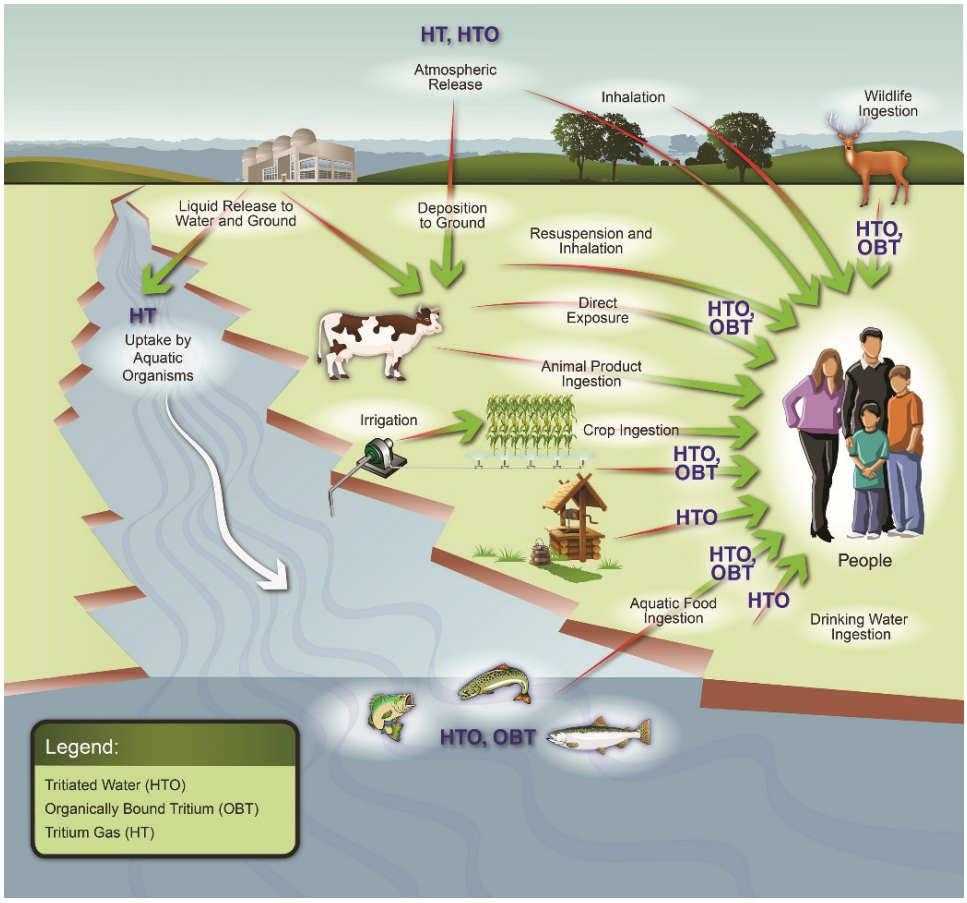

Figure 1. Environmental pathways considered for tritium dose calculations [7].

The Nuclear Regulatory Commission (NRC) and Environmental Protection Agency (EPA) have established three layers of radiation protection limits to protect the public. The first layer is the As Low As Reasonably Achievable (ALARA) objective and is stated in Appendix I to 10 CFR Part 50. The ALARA objective is 3 millirem (mrem) to the whole body and 10 mrem to any organ at the plant site boundary. If a nuclear power plant exceeds half of these radiation dose levels in a calendar quarter, the operator must investigate, initiate corrective actions, and report actions to the NRC within 30 days. The second layer is regulated by the EPA under 10 CFR 20.1301(e) and states radiation dose limits related to nuclear power are 25 mrem to the whole body, 75 mrem to thyroid, and 25 mrem to any other organ of any individual member of the public per year. The third layer is regulated by the NRC under 10 CFR 20.1301(a)(1) and limits radiation doses to 100 mrem per year for any individual of the public. Note that the average American receives a dose of 620 mrem per year as a cumulation of natural and man-made sources, and an abdomen x-ray is 60 mrem of dose [8]. Thus, exposure to radiation from nuclear power is minimal for the public under normal operation. However, converting dose to quantifiable tritium release from the facility is dependent on speciation, geographical, meteorological conditions, and site boundaries. Recent work calculated tritium release limits for various Department of Energy (DOE) site locations as it relates to dose at the site boundary [9]. The tritium release values ranged from 15.8–26.7 TBq/day which converts to 426–722 Ci/day to 0.04–0.07 g/day of tritium [9].

Tritium is produced in fission reactors through ternary fission of fuels as well as neutron reactions with elements in the coolant or moderator. Table 1 provides a summary of tritium production rates for various reactor types. The tritium produced in solid fuel is retained and not released to the environment except in accident scenarios or in the event of reprocessing. The primary source term for tritium in Light

Water Reactors (LWR) and other solid-fueled fission reactors is from ternary fission in the fuel elements. In Boiling Water Reactors (BWR), neutron capture by B-10 in the control rods leads to a secondary source term. Boric acid is added to Pressurized Water Reactor (PWR) reactor coolant system thus leading to a source term in the coolant-moderator system. In High Temperature Gas-cooled Reactors (HTGR), tritium is produced from lithium impurities in the graphite moderator. In Heavy Water Reactors (HWR), tritium is generated by neutron capture of deuterium in the heavy water moderator from the reaction $^{2}H(n,\gamma)^{3}H$, leading to significant tritium production. However, the tritium is contained in heavy water, thus limiting release pathways. In MSRs, tritium generation is dominated by neutronic interactions with the molten salt FLiBe. The activation and decay schemes that lead to tritium production from Li and Be are shown in Figure 2. Fluorine also produces tritium via the $^{19}F(n,t)^{17}O$ reaction, but at much smaller rates compared to ^{6}Li and ^{7}Li. Note that molten salt reactors that do not contain Li such as NaCl will not have the tritium production rates as FLiBe-based reactors.

Table 1. Estimated tritium production rates (Ci GWe^{-1} y^{-1}) in various reactor types.

Reactor Type	Total	Fuel	Coolant	Moderator	Reference
LWR -PWR	1.50×10^{4}	1.40×10^{4}	1.00×10^{3}	-	[10]
LWR-BWR	1.40×10^{4}	1.40×10^{4}	Low	-	[10]
HWR	1.46×10^{6}	1.40×10^{4}	5.00×10^{4}	1.40×10^{6}	[10]
HTGR	2.10×10^{4}	1.40×10^{4}	5.00×10^{3}	2.00×10^{3}	[10]
FHR[a]	BOL[c]: 9.24×10^{6} EQ: 2.67×10^{6}	-	-	-	[11]
MSR[b]	8.83×10^{5}	1.13×10^{4}	8.72×10^{5}	-	[12]

a. Calculated assuming 40% thermal efficiency and 100% availability.

b. Calculated assuming 100% availability.

c. BOL: Beginning of life. EQ: equilibrium.

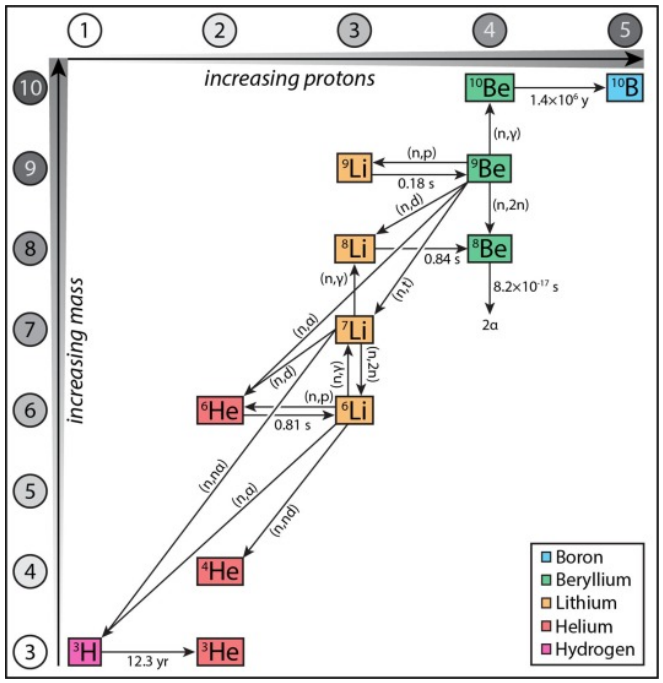

Figure 2. Activation and decay schemes of lithium and beryllium associated with tritium [13].

Tritium production is dominated by the presence of ^{6}Li due to its large cross section in the thermal neutron spectrum for the ^{6}Li(n,α)^{3}H reaction. MSR concepts plan to enrich with ^{7}Li to limit parasitic neutron loss through tritium production. However, ^{7}Li still produces tritium through several pathways and maintains a relatively high cross-section for the ^{7}Li(n,nα)^{3}H in the fast neutron spectrum. Neutron cross sections of reactions leading to tritium production are shown in Figure 3. For example, the MSR tritium production values reported in Table 1 are from calculations from the Molten Salt Breeder Reactor (MSBR) design study, which planned to use 99.99% ^{7}Li enrichment. Yet, 1170 Ci/day is calculated for the ^{7}Li(n,nα)^{3}H reaction, compared to 1210 Ci/day for the ^{6}Li(n,α)^{3}H reaction that resulted from ^{6}Li impurities [12]. For the FHR rates, 99.995 wt% ^{7}Li enrichment was used in the calculation [11].

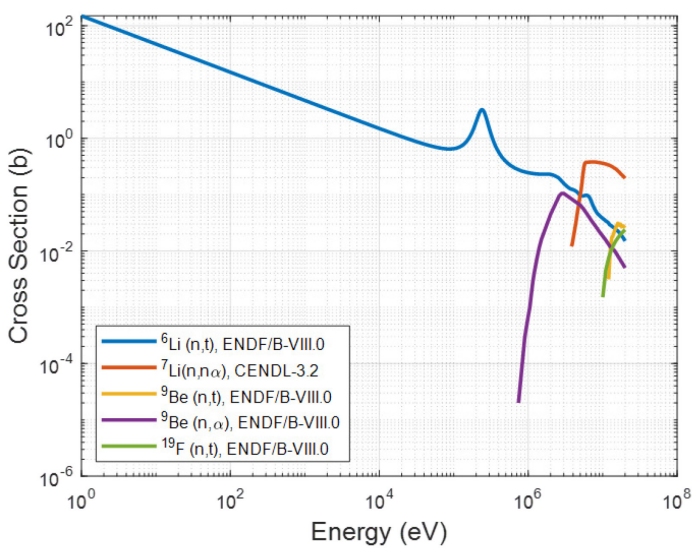

Figure 3. Neutron absorption cross section of nuclides relevant to tritium generation in molten salts [14].

1.2 Tritium Transport

The tritium transport phenomenon in molten salt reactors was the focus of a previous report by Humrickhouse and Fuerst [15, 16]. The primary tritium transport phenomena under investigation for molten salt reactors include:

- Transport properties in the salt phase: diffusivity, solubility, and speciation (TF, T_2, and LiT).
- Transport through and reactions with structural materials: diffusivity, solubility, dissociation ($T_2 \rightarrow 2T$), and recombination ($2T \rightarrow T_2$); as well as corrosion of structural materials through reactions with TF.
- Evolution into the gas phase either with two-phase bubble flow via sparging or from a free surface in a plenum or pump bowl.
- Uptake and trapping in core graphite.

2. MOLTEN SALT TRITIUM TRANSPORT EXPERIMENT DESIGN

The Molten Salt Tritium Transport Experiment is a forced convection fluoride salt loop with the capability of injecting hydrogen isotopes into a flowing salt and quantifying permeation rates through structural materials and evolution into gas-phase from free surfaces. The primary purpose of MSTTE is to provide validation data to elucidate tritium transport phenomena related to MSRs. However, the experiment is designed in a versatile manner to test tritium control and capture systems in future campaigns.

MSTTE will be constructed from the mating of a Copenhagen Atomics Pumped Salt Loop and an External Test Section as shown in Figure 4. A cross-section with major components listed is included in Figure 5. The main components of the Copenhagen Atomics Pumped Salt Loop include a salt tank, pump, flow meter, and pressure gauge. These are housed inside a furnace capable of operating to 700°C and are encapsulated by an inert Ar atmosphere enclosure with the instrumentation and controls inside. The pump exit and return are routed outside the enclosure and will be mated with the external test section. The main components of the external test section include the hydrogen injection system (HIS), permeation test section, plenum, sensors, vacuum system, and the gas distribution system. The external test section components are housed inside a ventilated safety enclosure. The loop will be constructed out of 316 stainless steel tubing with an outer diameter (OD) of 1.5 in. and wall thickness of 0.065 in. This allows the use of rotatable flanges designed and validated by Copenhagen Atomics.

The loop is designed for salt to passively drain to the salt tank inside the Copenhagen Atomics loop. Heated piping components are designed to withstand thermal expansion. Connections and breaks in salt-contacting piping is limited to minimize potential air exposure, but still allow versatility in the experiment. Flanges used in the experiment will have a localized inert Ar atmosphere by using a spiral-wound graphite gasket with 316SS casing on the salt-contacting flange portion and a metal O-ring forming an annulus. The annulus will be continuously flushed with argon providing the localized inert environment.

MSTTE will be commissioned with the molten fluoride salt FLiNaK and deuterium as surrogates for FLiBe and tritium in phase I. This facilitates ease of experiments and the ability to rapidly change configurations and test different control technology. Sited at the Safety and Tritium Applied Research (STAR) facility at Idaho National Laboratory (INL) enables the use of tritium and beryllium. Phase II of MSTTE consists of designing, constructing, and commissioning a salt-exchange and purification tank to switch between various molten salts (e.g., FLiBe) and provide in situ purification. This tank will be located underneath the external test section loop and in a separate enclosure. Addition of tritium diagnostics and delivery systems will enable lower detection limits for permeation and are planned as Phase III of MSTTE.

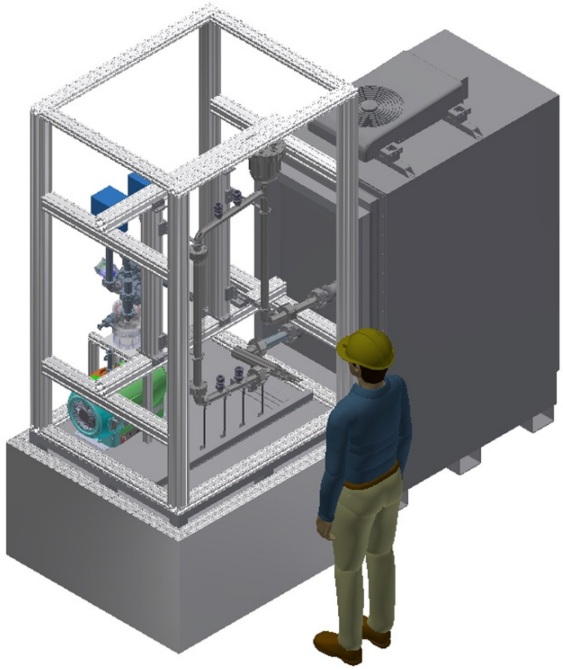

Figure 4. Computer Aided Design (CAD) rendering of MSTTE. The worker in the drawing is 6 ft for reference.

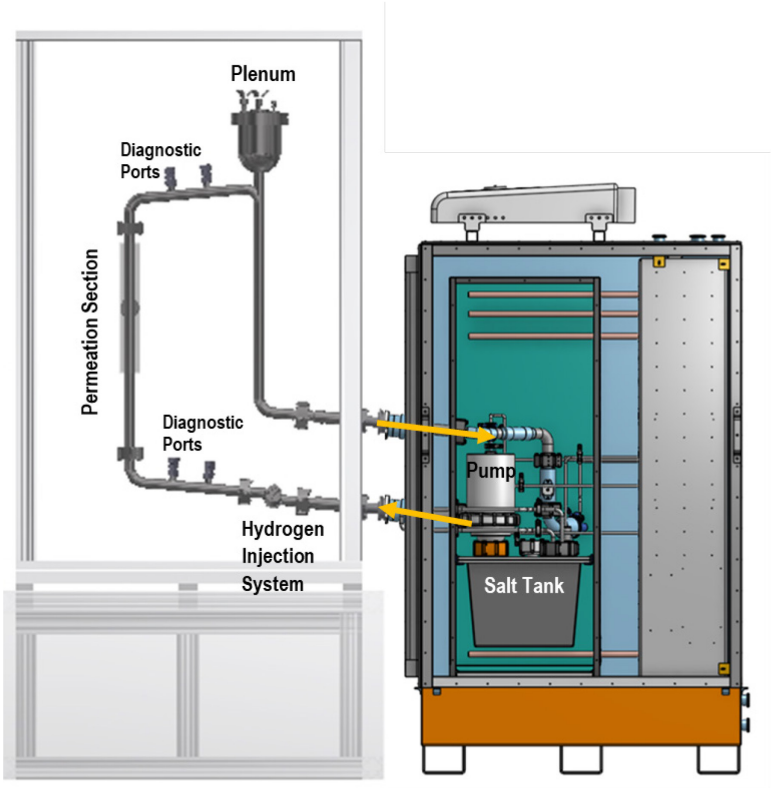

Figure 5. Cross section of MSTTE with major components listed.

2.1 Components

2.1.1 Copenhagen Atomics Pumped Portable Salt Loop

The pumped salt loop was ordered from Copenhagen Atomics in fiscal year (FY) 2022, see Figure 6 for a rendition of the pumped salt loop. The current status as of September 2023 is that the loop is being constructed at the Copenhagen Atomics facility and is undergoing commissioning tests with the molten salt FLiNaK (Figure 7). To meet INL safety standards, the loop is being evaluated by a Nationally Recognized Testing Laboratory (NRTL) to ensure compliance with the National Electrical Code and will be modified to meet specified codes. Delivery and installation of the loop at INL is anticipated in FY-24. The pumped salt loop is housed in an inert gas glovebox and consists of a pump, salt tank, and furnace heater, along with its instrumentation and controls. A cover gas composed of argon is supplied to the salt tank as well, as is the inert gas inside the enclosure. The loop is shipped with purified FLiNaK supplied by Copenhagen Atomics. Ports are routed through the enclosure and are connected to the external test section. The pump loop will be mated to the test section loop enclosure. The technical specifications of the salt loop include:

- Electrical Power: 22kW power, 32A, 3 phase, 380 VAC
- Maximum temperature of 700°C
- Maximum flow rate: 300 LPM
- Minimum flow rate: 50 LPM
- Maximum salt load: 100 L
- Initialization and heat-up time: 12 hours
- Loop weight: 1000 kg.

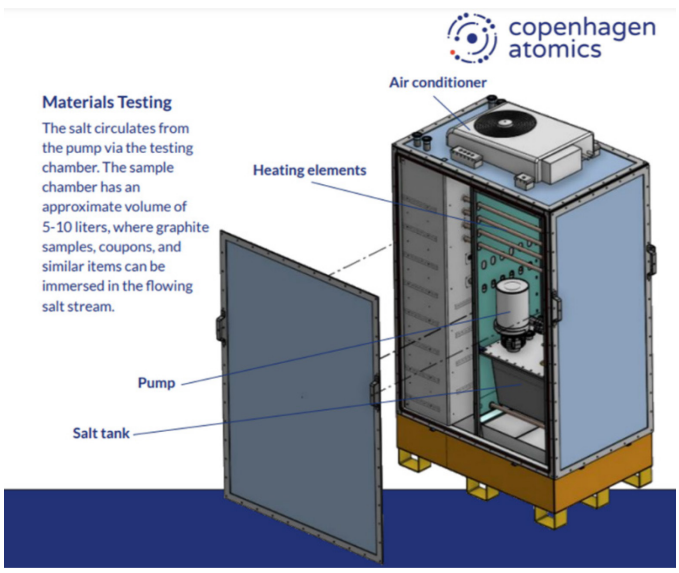

Figure 6. Pumped salt loop from Copenhagen Atomics [17].

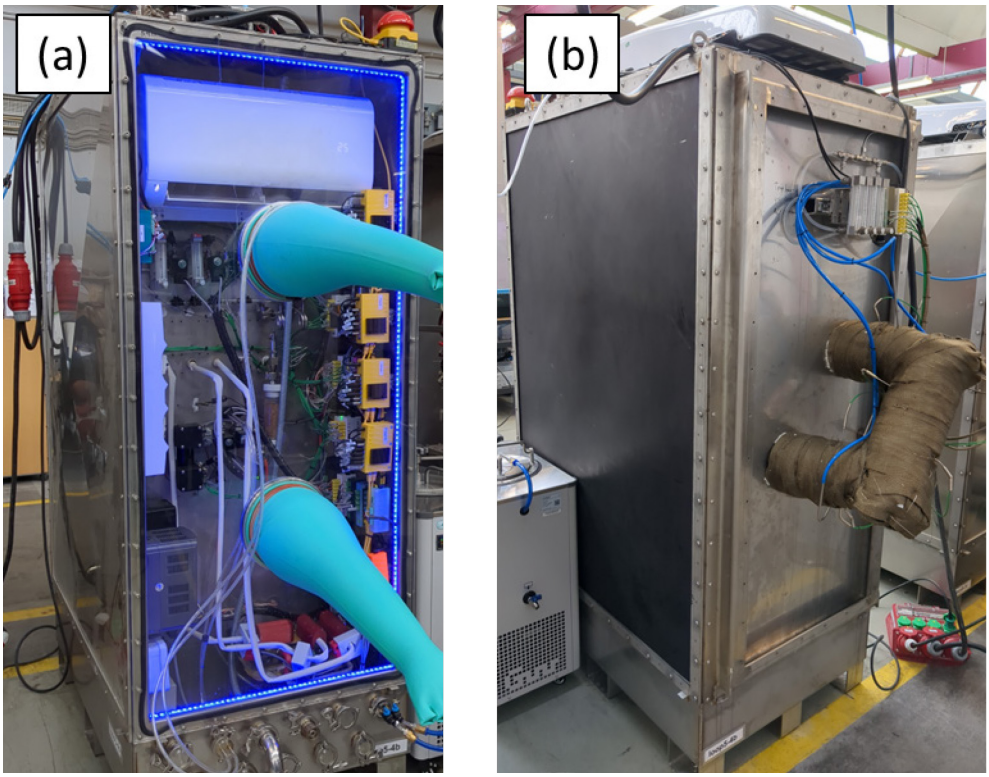

Figure 7. Front (a) and back (b) of as-built Copenhagen Atomics Salt Loop for MSTTE at the Copenhagen Atomics facility.

2.1.2 Hydrogen Injection System

The Hydrogen Injection System (HIS) is designed as a "mass exchanger" in a shell-and-tube configuration facilitating permeation of hydrogen into the molten salt. Molten salt flows on the shell-side and hydrogen isotopes are supplied with a set pressure inside the tubes. The hydrogen isotopes permeate through the tubes and into the molten salt in a uniform and controlled manner. Permeation rates are measured by pressure drop in a calibrated volume with high accuracy capacitance manometers and is discussed in Section 2.1.5. The HIS design has been updated from a previous iteration to reduce pressure losses and to allow the component to self-drain (Table 2, Figures 8, and Figure 9).

Table 2. Design Parameter Changes for the HIS.

Parameter	Original HIS	Updated HIS
Shell	2 inch 316 SS	1.5 inch 316 SS
Entrance	90° Port	90° Bend
Exit	90° Port	90° Wye Bend
Number of Injection Tubes	Five	Three
Tube Diameter	0.25 inch 316 SS	0.25 inch 316 SS
Tube Orientation	Square Pitch 0.75 inch	Triangular Pitch 0.7 inch
Tube Length	10 inch	7.5 inch
Fully Drains	No	Yes
Pressure Loss (FLiNaK)	7.83 kPa	3.56 kPa
Pressure Loss (FLiBe)	7.71 kPa	3.91 kPa

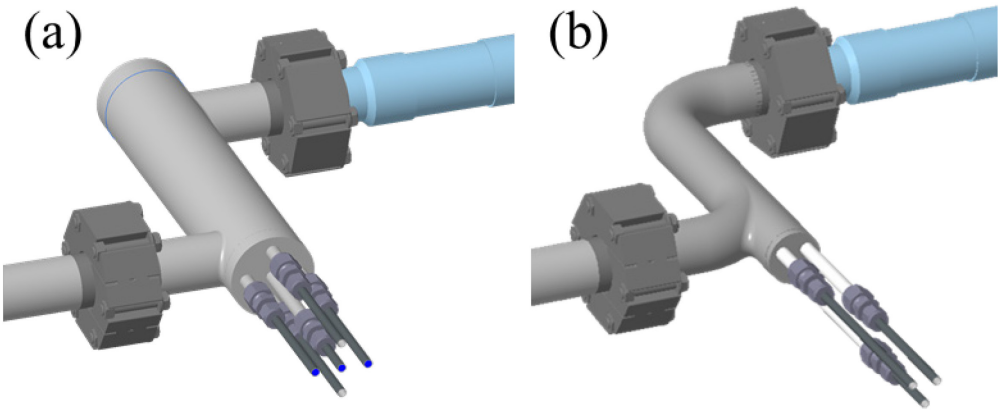

Figure 8. (a) Original HIS with five-tube design and (b) updated HIS including three-tube design.

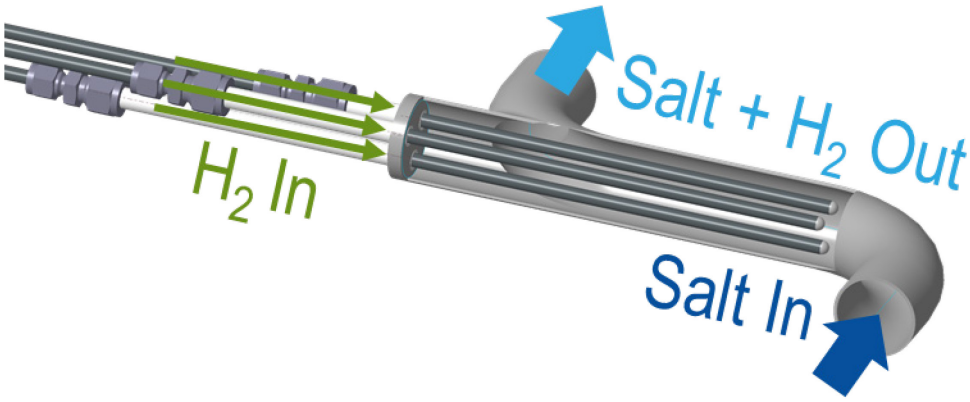

Figure 9. Section view of the HIS.

Given the reduction in size of the new injection system, the total permeation rate was compared through each design (Figure 10). A numerical advection-diffusion model of hydrogen flux through the pipe wall was evaluated to ensure that prototypic concentration of hydrogen can be achieved in the loop. This model (Appendix A) shows that the HIS still can achieve prototypic concentrations with sub-atmospheric hydrogen pressures. Appendix B overviews weld specifications for ports and extrusions in the loop piping for this and other components.

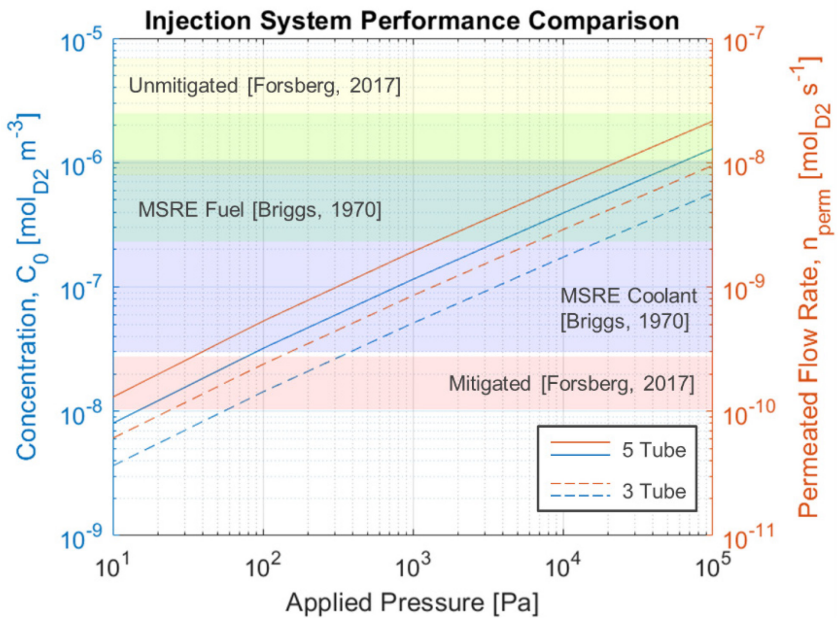

Figure 10. Permeation calculations for both five-(original) and three-(updated) tube designs.

2.1.3 Permeation Test Section and Vacuum Diagnostics

The first experimental campaign will investigate deuterium permeation through the structural and heat exchanger material 316 stainless steel. The permeation test section consists of a 316 stainless steel tube with a length of 18 inch, outer diameter of 1.5 inch, and wall thickness of 0.065 inch (Figure 11). The tube sample is encased in a 316 stainless steel shell that can be continuously evacuated during experiments. The inner tube will be heated with an inserted infrared heat lamp. The salt flows through the inside of the sample tube. Hydrogen dissolved in the salt diffuses through the metal tube wall, and the permeation rate will be monitored with two calibrated quadrupole mass spectrometers (QMS) supplied by MKS Instruments. An e-vision 2 QMS will scan 1–100 amu, and a customized microvision-2 QMS will scan 1–6 amu for hydrogen speciation.

The permeation flow rate range detectable with the QMS is estimated to be from 10^{-13} mol s^{-1} to 10^{-9} mol s^{-1} from previous experience with these instruments. Results from the advection-diffusion analytical model suggests that measurable permeation rates from the test section are achieved with prototypic concentrations (Figure 12). Additionally, care must be taken to consider the permeation rate through the 316 stainless steel shell when analyzing MSTTE permeation data.

Two tasks remain for the permeation test section: (1) assurance of a fully developed flow field for the salt (focus of Section 4), and (2) incorporation of an infrared (IR) heater lamp to heat the in-vacuo piping. Both these tasks are currently underway and will be complete, constructed, and operational in the FY-24.

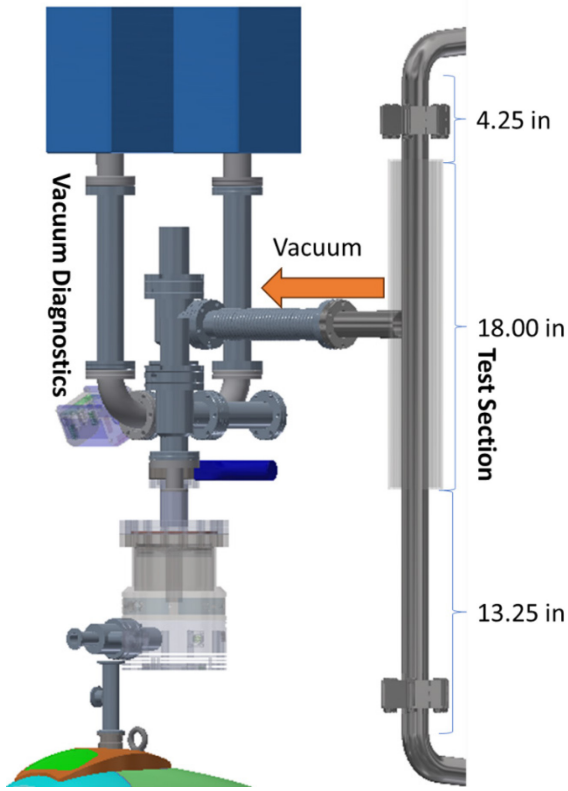

Figure 11. Permeation test section, length scales, and diagnostics.

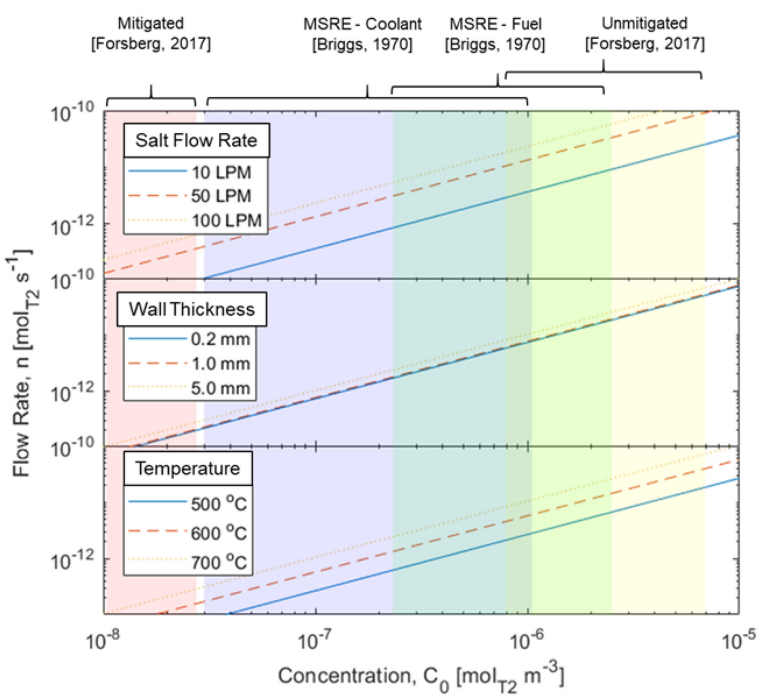

Figure 12. Analytical solution for permeated hydrogen flow rate through test section with varying experimental variables.

2.1.4 Plenum

The plenum is located at the top of the loop and serves a multifunctional purpose. The plenum serves as a free surface for salt volumetric expansion as well as tritium transport from salt to gas-phase where it is collected in the purge gas. The flanged lid provides ports for vacuum evacuation during loop bakeout, Ar cover gas, thermocouples, and extra ports reserved for collaborations with diagnostics such as Laser Induced Breakdown Spectroscopy (LIBS) [18], Raman probes [19], electrochemical sensors [20], and triple bubbler systems [21].

The current plenum design is shown in Figure 13. The bottom of the plenum is a wye branch into the primary test loop tubing and expands into a 6-inch OD hemispherical bottom. The distance from the tee to the lid is 8.425 inch. The lid is fabricated from an 8-inch Conflat® flange (CF) with ports for six DN16CF flanges and one DN35CF-DN40CF flange. Currently, two DN16CF flanges are planned for thermocouples that act as temperature measurement as well as salt pool height, one DN16CF is reserved for Ar cover gas, and another flange is reserved for vacuum pumping. Two DN16CF ports and the DN35CF-DN40CF port are reserved for future diagnostic incorporation. The bottom of the plenum will be heated, so a gas-cooled jacket may be required to keep the CF gasket < 450°C. Additional diagnostics can be inserted in the four ports (two top and two bottom) that are located on the top and bottom legs of the loop, respectively.

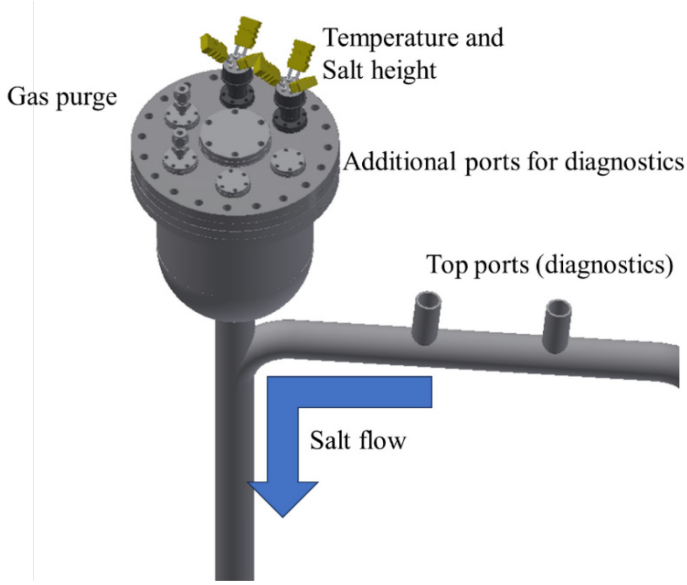

Figure 13. CAD of MSTTE plenum.

2.1.5 Gas Distribution System

A gas distribution system supplies a set pressure of hydrogen (deuterium or tritium) to the HIS, an argon purge gas to the plenum with controlled back pressure, and supply flanges with a set flow rate cover gas of argon. The overview of the gas distribution system is visualized in Figure 14.

The HIS includes an Alicat dual-valve pressure control with 30 pisa maximum pressure to set the pressure in the injection system permeator tubes. 5000 Torr and 100 Torr heated MKS high-accuracy capacitance manometers are used to measure the set pressure in the HIS. A turbomolecular pump and dry scroll pump from Agilent are used to evacuate the system between experiments. The plenum purge system includes an Alicat 5 SPLM mass flow controller and an Alicat pressure controller to set for back pressure control. The pressure is monitored with an Ashcroft absolute pressure transducer. A calcium carbonate getter bed is used to ensure containment of any trace potential HF generated in the experiment. The gas stream can then be routed to a gas chromatograph for analysis or straight to facility exhaust.

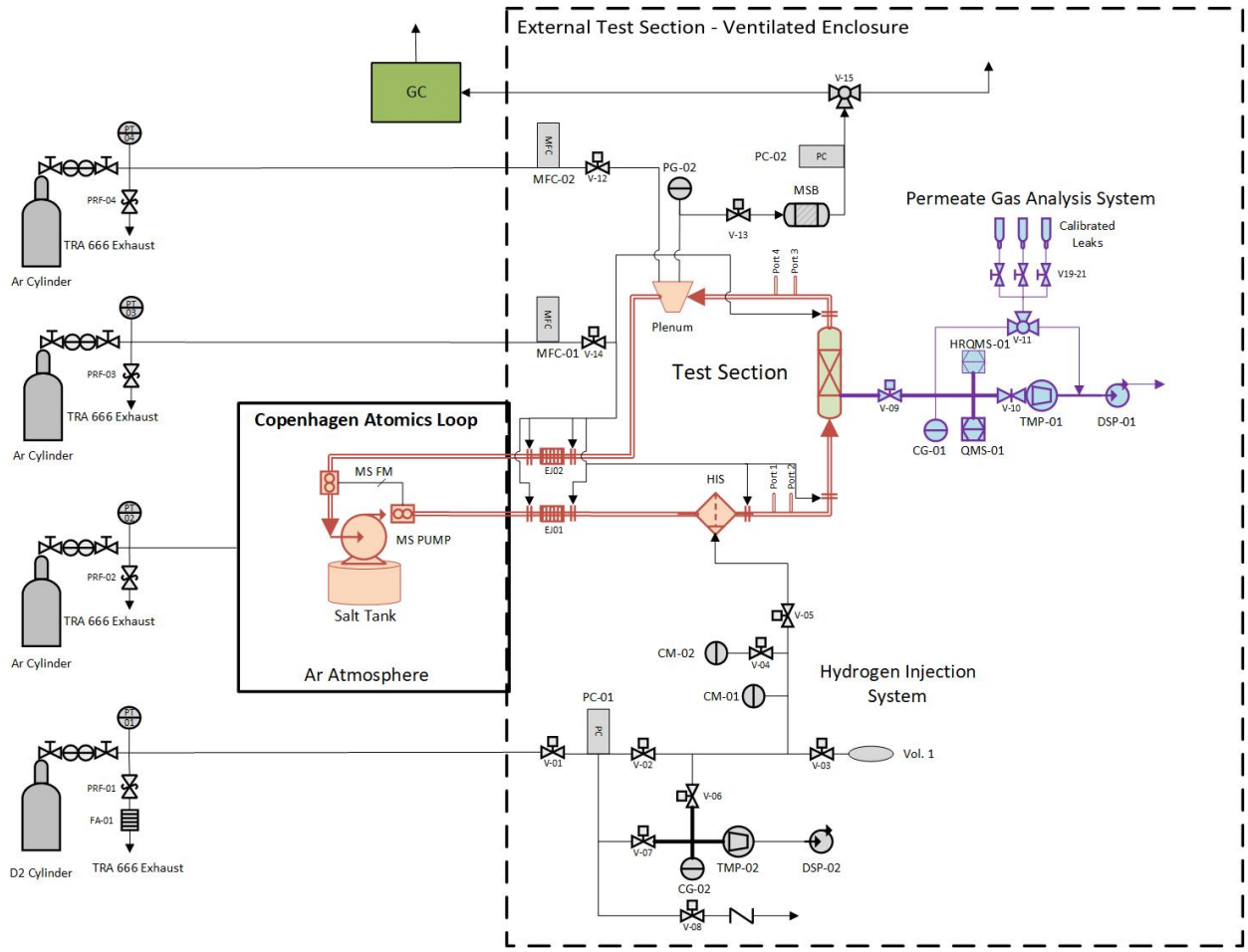

Figure 14. Piping and Instrumentation Diagram (P&ID) for MSTTE.

2.2 External Test Section Pressure Drop

The design of the test loop included calculations of pressure losses through individual components as a result of pipe geometry and friction. The evaluation resulted in an overall pressure differential between the inlet and outlet, used to determine the sufficiency of the Copenhagen Atomics pump. Copenhagen Atomics specifies a maximum volumetric flow rate of 200 kPa, with typical operation of 100 kPa at 200 LPM. Given the difference in material properties of both FLiNaK and FLiBe, pressure drop for both was evaluated at 600°C, the lower operating temperature where viscosity and pressure loss will be the greatest for both fluid. The friction of tube walls, in addition to momentum losses due to the geometry in bends, constrictions, and wye branches were evaluated for pressure losses. These pressure calculations include the updated hydrogen injection system. The fluid flow parameters are included in Table 3.

Table 3. Fluid flow parameters for 100 LPM and loss coefficients for components.

Parameter	Equation/Symbol	FLiNaK	FLiBe
Temperature	T	600°C	600°C
Density	ρ	2034 kg/m^2	1987 kg/m^2
Dynamic Viscosity	μ	4.19×10^{-3} Pa•s	5.50×10^{-3} Pa•s
Volumetric Flow Rate	$\dot{V}$	100 LPM	100 LPM

Parameter	Equation/Symbol	FLiNaK	FLiBe
Pipe ID	d	0.0348 m	0.0348 m
Velocity	$v = \frac{\dot{V}}{\pi(d/2)^2}$	1.75 m/s	1.75 m/s
Reynolds Number	$Re = \frac{\rho v d}{\mu}$	29600	14200
Roughness SS316	$\in$	5×10^{-7} m	5×10^{-7} m
Friction Factor	$f = \left\{-1.8 \log\left[\left(\frac{\in}{3.7d}\right)^{1.11} + \frac{6.9}{Re}\right]\right\}^{-2}$	0.0324	0.0281
Friction Pressure Losses	$\Delta P = \frac{f L \rho v^2}{2d}$	See Table 4 for Component pressure drops with Parameters Length L Angle α Radius r Plate Area Ratio λ	
Loss Coefficient for Bends	$K = f\alpha\frac{r}{d} + (0.1 + 2.4f)sin\left(\frac{\alpha}{2}\right) + \frac{6.6f\left(\sqrt{sin\left(\frac{\alpha}{2}\right)} + sin\left(\frac{\alpha}{2}\right)\right)}{\left(\frac{r}{d}\right)^{\frac{4\alpha}{\pi}}}$		
Loss Coefficient for Wye/Tee	$K = 0.42sin\left(\frac{\alpha}{2}\right) + 2.56sin^3\left(\frac{\alpha}{2}\right)$		
Loss Coefficient for Flow Conditioner	$K = \frac{[0.707(1-\lambda)^{0.375} + 1 - \lambda]^2}{\lambda}$, $\lambda = \frac{open\ flow\ area}{pipe\ cross\ section}$		
Pressure Loss for Geometry	$\Delta P = K\frac{\rho v^2}{2}$		

With these parameters, the equations were applied with the specific geometry of each individual component to get a total pressure drop for the entire loop. Each section (Figure 15) was also assessed individually to determine where losses could potentially be reduced, and pressure losses are reported in Table 4.

Table 4. Pressure loss through components with 100 LPM salt flow rate at 600°C.

Component Type	Geometry Parameters	Loss Coefficient		Pressure Drop (Pa)	
		FLiNaK	FLiBe	FLiNaK	FLiBe
Pump Exit					
Exit Bend	$r = 0.0508\ m$, $\alpha = 115°$	0.356	0.411	1110	1250
Exit Attachment (Straight)	$L = 0.4\ m$			841	1010
Exit Bellows (Straight)	$L = 0.152\ m$			320	375
Flange 1 (Straight)	$L = 0.077\ m$			161	189
Pump Exit Total				**2430**	**2830**
Hydrogen Injection System					
HIS Inlet leg (Straight)	$L = 0.025\ m$			53.4	62.7
HIS Inlet Bend	$r = 0.0508\ m, \alpha = 90°$	0.339	0.393	1060	1200
HIS Body (Straight)	$L = 0.101\ m$			214	251

Component Type	Geometry Parameters	Loss Coefficient		Pressure Drop (Pa)	
		FLiNaK	FLiBe	FLiNaK	FLiBe
HIS Exit Wye	$\alpha = 51°$	0.385	0.390	1203	1203
HIS Exit Bend	$r = 0.0508\ m, \alpha = 90°$	0.313	0.370	978	1130
HIS Exit Leg (Straight)	$L = 0.025\ m$			53.4	62.7
HIS Total				3560	3910
Lower Leg					
Flange 2 (Straight)	$L = 0.077\ m$			161	189
Lower Leg (Straight)	$L = 0.330\ m$			694	815
Lower Leg Bend	$r = 0.0508\ m, \alpha = 85°$	0.335	0.389	1050	1190
Lower Vertical (Straight)	$L = 0.152\ m$			53.4	62.7
Flange 3 (Straight)	$L = 0.077\ m$			161	189
Lower Leg Total				2116	2442
Test Section					
Flow Conditioner (Plate	$\lambda = 0.593$	2.35	2.35	7340	7160
Test Section (Straight)	$L = 0.737\ m$			1548	1818
Flange 4 (Straight)	$L = 0.077\ m$			161	189
Test Section Total				9046	9169
Top Leg					
Top Leg Vertical (Straight)	$L = 0.025\ m$			53.4	62.7
Top Leg Bend 1	$r = 0.0508\ m, \alpha = 85°$	0.335	0.389	1047	1189
Top Leg (Straight)	$L = 0.152\ m$			748	877
Top Leg Bend 2	$r = 0.0508\ m, \alpha = 48°$	0.313	0.368	978	1120
Top Leg Wye	$\alpha = 51°$	0.385	0.385	1203	1170
Top Leg Down (Straight)	$L = .686\ m$			1440	1690
Top Leg Bend 3	$r = 0.0508\ m, \alpha = 85°$	0.335	0.389	1050	1190
Top Leg Bottom (Straight)	$L = .076\ m$			160	188
Top Leg Total				6680	7490
Pump Return					
Flange 5 (Straight)	$L = 0.077\ m$			161	189
Return (Bellows)	$L = 0.152\ m$			320	375
CA Return Connection (Straight)	$L = 0.45\ m$			946	1140
CA Return Bend	$r = 0.0508\ m, \alpha = 38°$	0.313	0.370	978	1130
CA Return Leg (Straight)	$L = 0.315\ m$			662	796
CA Return Drop Bend	$r = 0.0508\ m, \alpha = 90°$	0.339	0.393	1060	1199
CA Return Drop (Straight)	$L = 0.465\ m$			977	1175
Pump Return Total				5102	5998
Loop Total Pressure Drop				28930	31840

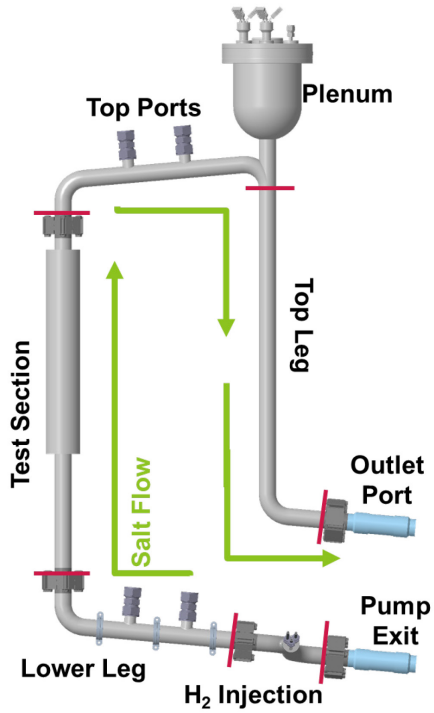

Figure 15. External test section with components labeled.

The calculations were repeated for the pump's nominal operating flow rates from 100 LPM to 300 LPM (Figure 16). Note that the minimum flow rate is 50 LPM and not plotted. While the maximum specification of 200 kPa is exceeded at higher rates of flow, these flow rates are not expected in normal operation of the pump. With roughly 100 kPa of loss at 200 LPM in this loop, as outlined by Copenhagen Atomics for typical operation, the test loop geometry is suitable for usage with this pump. Note that this sectionalized analysis corresponds well with the results from analysis with the System Analysis Module in Section 3.

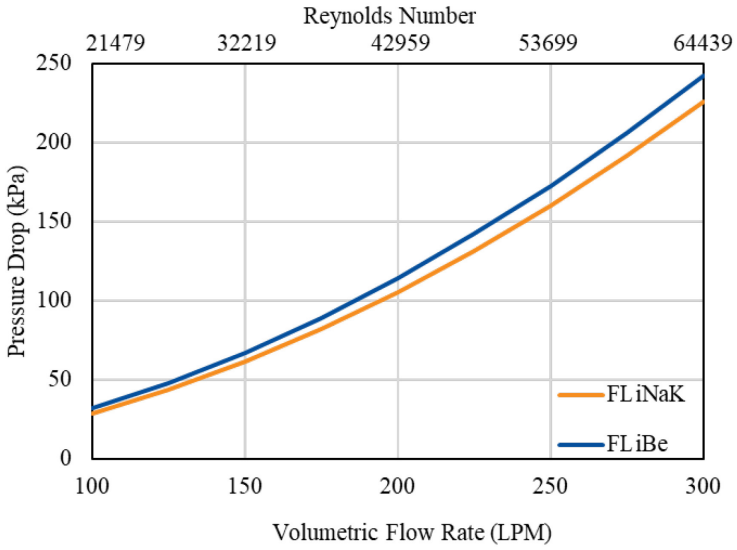

Figure 16. Pressure drops through the external test section for FLiNaK and FLiBe as a function of salt flow rate at 600°C.

2.3 Stress Analysis

2.3.1 Loop Stress Analysis

The external test section is fixed to bellows connected to the Copenhagen Atomics pump loop. The high temperature operation (700°C max) causes thermal expansion during start up as the loop heats up from room temperature. The support structure of the loop has been designed with mounts that slide with the loop on rails or allow for the loop to slide through the mount freely. This mitigates stress on loop supports and on the loop itself. However, with the fixture of the bellows at the inlet and outlet of the loop, the expansion will cause bending within the tube. A finite element model was created using the BISON fuel performance code in the MOOSE framework utilizing thermo-mechanical properties of 316 SS. The model was solved as a reference residual problem with nonlinear absolute tolerance.

The MSTTE loop geometry was mapped to a linear tetrahedral mesh using Cubit 16.08. The model geometry is unstressed at room temperature (21°C). The maximum thermal expansion occurs with a peak temperature of 700°C in the molten salt. The temperature was applied as a linear function of time, reaching peak temperature after an 11-hour start-up period. The simulation continued to evaluate any time-dependent creep effects over 2000 hours at temperature. The entrance and exit of the loop are fixed at a specified node, allowing thermal expansion of the pipe. The mounts along the base of the loop are represented by fixed nodes in 2 axes, allowing for the loop the expand radially and by sliding through the mounts on the free axis.

The peak von Mises stress in the loop is 25 MPa as shown in Figure 17. At 700°C, the yield stress of 316 Stainless Steel is 115 MPa, giving the loop a factor of safety of 4.6. The maximum thermal displacement magnitude in the loop after 2000 hours at 700°C was 1.8 cm from resting conditions at the elbow above the test section, which is also where the maximum stresses are predicted. The modeled stress may be artificially high due to the tetrahedral elements used in the mesh, which are less able to adjust to changes in geometry than hexahedral elements are; nevertheless, the prediction is conservative.

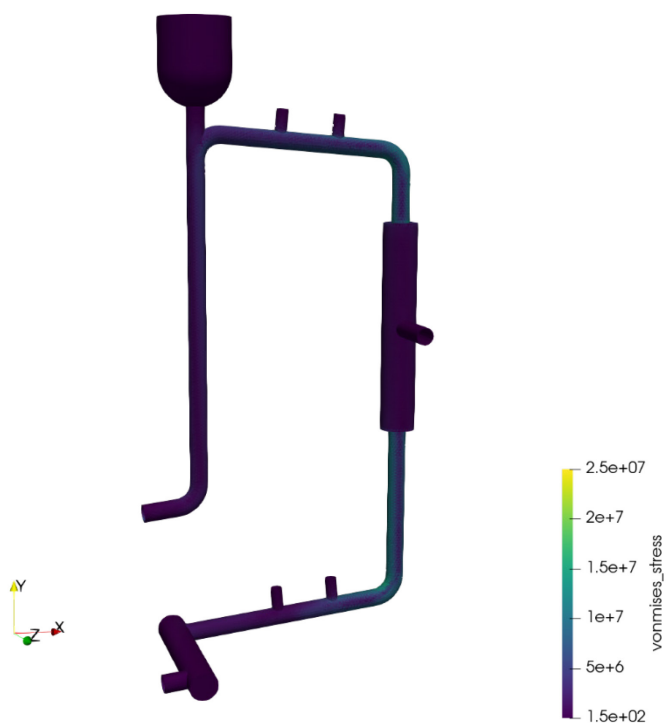

Figure 17. Modeled von Mises stress of the MSTTE loop at 700°C.

2.3.2 Support Stress Analysis

The support structure on the lower leg of the mount is designed to support the entire weight of the load, while the rest of the structure is used only for stabilization in the z-direction per Figure 17. The mounts will distribute the estimated 33 kg based on analysis of geometry in CAD. Initial designs included rods mounted from below the loop to the base of the structure. The incorporation of a drip pan was necessary for containment of molten salt in the event of failure or leakage from the loop, but eliminated mounting points underneath the loop. To support the loop, mounting points from the side of the loop will be utilized, with mounting rods undergoing a cantilever loading. The high operating temperature of the loop and the surrounding insulation mounting is in direct contact will cause creep of the mounts. A finite element model was used to evaluate the strength required of the mounting rod as well as the deflection seen.

The model was generated in MOOSE using BISON thermo-mechanical material modeling of 316 SS. The mounting system consists of an anchor that attaches the rod perpendicularly to the 80/20 framing. An M12 6.5-inch threaded rod (316 SS) extends to the loop, where an adapter attaches it to a clamping hanger (Figure 18). For the finite element model (Figure 19), the adapter and rod are considered one solid component under the assumption the interface of the two components does not affect the peak stress at the base of the rod. A smooth rod with the inner diameter of the M12 threads was used to simplify geometry, as unused threads will not affect strength, and the difference in surface area underestimates convection and cooling of the rod. The CUBIT-generated mesh utilizes linear hexahedral elements with a consistent and symmetric cross section through the length of the rod.

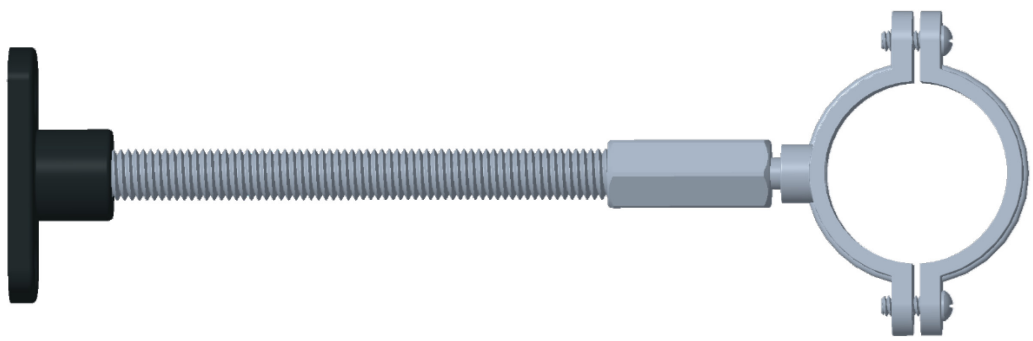

Figure 18. Side mounting geometry.

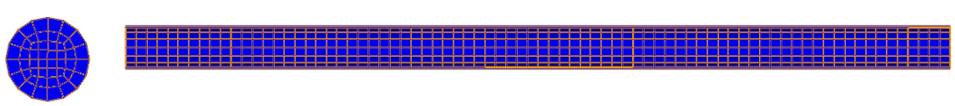

Figure 19. Mesh geometry of side mounting geometry.

The unbraced model did not exceed the yield stress of 316 SS but had a 1.2-mm displacement in bending that would only get worse with fatigue effects due to thermal cycles on the loop, especially when insulation is added to the rod. To reduce displacement and distribute stress concentrated at the mount, an angled brace of 80/20 was attached at 45° below the rod (Figure 20). The updated model reduced overall stress and deflection, even with the addition of insulation raising the average temperature of the rod (Figure 21 and Table 5).

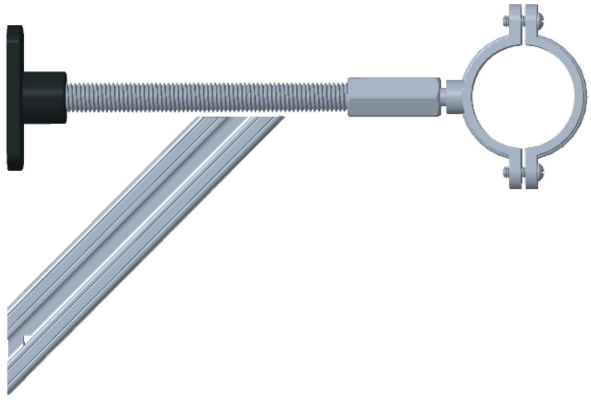

Figure 20. Example of braced rod configuration.

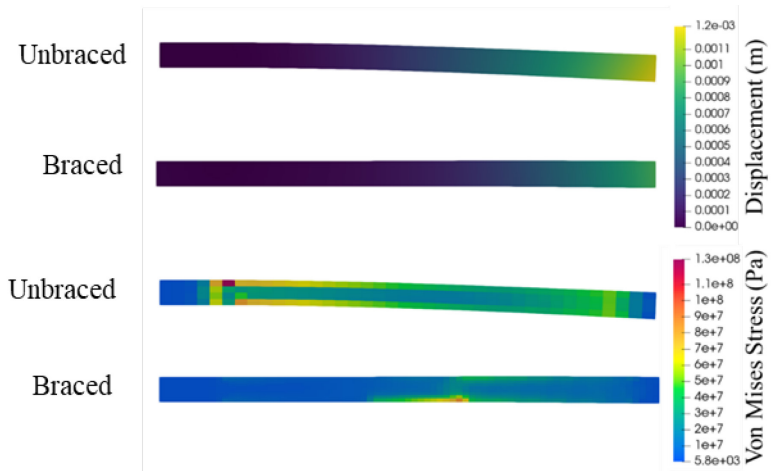

Figure 21. Unbraced (top) and braced (bottom) rod displacement, stress, and temperature.

Table 5. Brace model summary.

	Unbraced	Braced
Peak Displacement	1.2 mm	0.9 mm
Peak von Mises Stress	130 MPa	86 MPa

3. MSTTE TRITIUM TRANSPORT ANALYSIS

The System Analysis Module (SAM) [22] is an advanced system analysis tool under development at Argonne National Laboratory for advanced non-LWR reactor safety analysis. It aims to provide fast-running, modest-fidelity, whole-plant transient analyses capabilities, which are essential for fast turnaround design scoping and engineering analyses of advanced reactor concepts. SAM takes advantage of advances in physical modeling, numerical methods, and software engineering to enhance its user experience and usability. It utilizes the object-oriented computational framework MOOSE [23] along with its underlying meshing, finite-element library, linear, and non-linear solvers to leverage modern advanced software environments and numerical methods.

The ability to track various species (e.g., delayed neutron precursors and their decay heat, tritium, heavy metal particles, and fission products) in the primary cooling system of reactor systems is key for MSR transient simulation as well as source term evaluation for other advanced reactors. A mass transport modeling capability was previously implemented in SAM based on the general scalar transport model to support point kinetics modeling of liquid-fueled reactor concepts, where it is necessary to track the drift of delayed-neutron precursors [22]. In FY-22, this capability was extended to capture source term phenomena in advanced reactors, with an initial focus on tritium transport. Tritium is a relevant source term in reactors utilizing lithium-bearing salt coolants such as the FHR concept [24]. The direct integration of this model within SAM provides for directly informed velocity profiles of tritium and local temperatures throughout the system, thus improving accuracy in material property evaluation and overall source term analysis methodology.

3.1 Tritium Transport Model in SAM

The primary scope of the species transport model in SAM is to capture source term phenomena at an engineering scale that is relevant to system-level analysis. The governing equation for passive scalar transport in the fluid is given below, in which the second and third terms on the left-hand side represent advection and molecular diffusion, the fourth term represents nuclear decay, and the source term is defined on the right-hand side of the equation;

$$\frac{\partial \rho c_i}{\partial t} + \nabla \cdot (\rho u c_i) - \nabla \cdot (\mathrm{D}_i \, \nabla c_i) + \lambda \rho c_i = S_i \tag{1}$$

where ρ is the bulk fluid density [kg/m^3], c_i is the scalar particle (species) mass concentration for each species i [mol/kg$_{\mathrm{fluid}}$], u is the fluid velocity [m/s], D_i is the diffusion coefficient [m^2/s], λ_i is the decay constant [s^{-1}], and S_i is the volumetric source term [mol/m^3]. The species transport equation is solved together with the one-dimensional fluid conversation equations, incorporating the same Streamline-Upwind/Petrov-Galerkin and Pressure-Stabilizing/Petrov-Galerkin stabilization schemes used in the 1-D fluid model [22]. With regards to tritium (and hydrogen isotope) transport, SAM does not currently implement a model for speciation within the salt and assumes most of the tritium will exist as T_2 rather than TF.

Tritium and other hydrogen isotopes in their monoatomic state are found to permeate through metals and retain within graphite [25]. This transport of tritium within metals can be predicted as diffusion of species concentration c_d [mol/m^3] with diffusivity D according to Fick's law:

$$\frac{\partial c_d}{\partial t} - \nabla \cdot (\mathrm{D} \, \nabla c_d) = 0 \tag{2}$$

In graphite, the behavior of tritium interaction can be modeled by various processes of diffusion, trapping, and de-trapping within the pore and grain structure, which is also captured in SAM [24].

Transport of a species from a fluid region into a solid region and vice-versa can be considered as a convective mass transfer coupling the diffusion and advection processes occurring in each domain [11].

The convective flux of a fluid species from the bulk to the surface can be modeled as the concentration gradient multiplied by a mass transfer coefficient:

$$j_{c_f} = M_{\mathrm{W}} \cdot \left(\rho_{\mathrm{fluid}}\, c_{f,\mathrm{bulk}} - c_{f,surface}\right) \tag{3}$$

where j_{c_f} is the species flux [mol/m^2-s], M_{W} is the mass transfer coefficient [m/s], $c_{f,bulk}$ is the fluid species mass fraction in the bulk region [mol/kg], and $c_{f,surface}$ is the fluid species concentration at the wall surface [mol/m^3]. The mass transfer coefficient can be determined from various correlations depending on the flow parameters. Since the local heat transfer coefficient $\boldsymbol{h}$ is readily available from the 1-D thermal-fluid model, the Chilton-Colburn analogy can be applied to correlate the local mass transfer coefficient [26]:

$$M_w = \boldsymbol{h} \cdot \frac{\mathrm{D}}{k}\left(\frac{\mathrm{Sc}}{\mathrm{Pr}}\right)^{1/3} = \boldsymbol{h} \cdot \frac{\mathrm{D}^{2/3}}{k^{2/3}\left(\rho c_p\right)^{1/3}} \tag{4}$$

where D is the diffusivity of the species [m^2/s], and k, ρ, and c_p are thermophysical properties of the bulk fluid. At the fluid-solid interface, the conserved molar diffusive flux on the solid structure side (monoatomic tritium) is twice the molar flux on the fluid side (T_2):

$$2 \cdot M_{\mathrm{W}} \cdot \left(\rho_{\mathrm{fluid}}\, c_{f,\mathrm{bulk}} - c_{f,surface}\right) = \mathrm{D}\, \nabla c_d \tag{5}$$

The concentration of the species in the fluid at the surface of the solid can be determined by its solubility in the fluid as governed by Henry's law and the solubility of the diffused species in the solid as governed by Sievert's law [11]:

$$p_{c_f} = \rho_{fluid}\, c_{f,surface}/\mathrm{K}_{\mathrm{Henry}} = \left(c_{d,wall}/\mathrm{K}_{\mathrm{Sievert}}\right)^2 \tag{6}$$

where p_{c_f} is the partial pressure of the fluid species [Pa], K_{Henry} is Henry's law solubility constant [mol/m^3-Pa], $c_{d,wall}$ is the diffused species concentration at the outer surface of the solid [mol/m^3], and $K_{Sievert}$ is Sievert's law solubility constant [mol/m^3-Pa$^{1/2}$]. A selection of species material properties is available within SAM, with relevant properties outlined in Table 6.

Table 6. Species material properties included in SAM's built-in library that are used in the MSTTE facility model.

Species	Bulk Material	Property Model	Reference
T_2	FLiBe	$\mathrm{D} = 9.3 \times 10^{7} \mathrm{e}^{-42/\mathrm{RT}}$	[27]
		$\mathrm{K_H} = 2.714 \times 10^{-8} \mathrm{e}^{4.235 \times 10^{-3}(\mathrm{T}-273.15)}$	[11, 28]
T ("tritium")	316 SS	$\mathrm{D} = \sqrt{1/3} \cdot 6.32 \times 10^{-7} \mathrm{e}^{-47.8/\mathrm{RT}}$	[29]
		$\mathrm{K_S} = 0.427 \mathrm{e}^{-13.9/\mathrm{RT}}$	[29]

3.2 Verification with an Analytical Permeator Model

Verification of tritium transport modeling using the TRANSFORM library was performed by Rader et al. [30], in which the analytical solution for tritium concentration profiles in a proposed permeator extraction system were derived. The permeator is represented as a simple thin-walled nickel pipe with FLiBe as the carrier fluid. Dimensions, constant properties, constant flow boundary conditions, and vacuum/sweep gas boundary at the outer wall pipe surface are listed below in Table 7. This was modeled in SAM using a *PBPipe* component as a steady-state simulation to verify the accuracy of the implemented tritium transport model with the analytical solution, as demonstrated in Figure 22.

Table 7. SAM model parameters for a proposed FliBe-nickel permeator extractor [30].

Permeator materials	FLiBe / Ni	Inlet tritium (mol/m^3)	1.0
Tube length (m)	50.0	Mass Transfer Coefficient (MTC) (mm/s)	0.171
Tube ID (mm)	25.4	Wall Temp. BC	Adiabatic
Tube wall thickness (mm)	0.25	Wall Species BC	$c_{surf} = 0.0$
Fluid velocity (m/s)	2.5	Axial nodes	50
Temperature (K)	973.15	Radial (wall) nodes	5

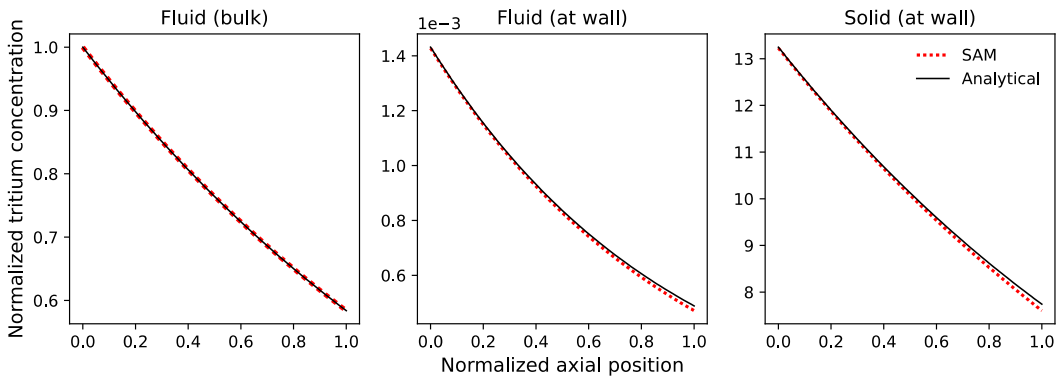

Figure 22. Comparison of normalized tritium concentrations in the fluid bulk region (left), in the fluid near the wall (center), and in the solid at the wall surface (right) as predicted by SAM versus the analytically derived concentration profiles [30].

3.3 SAM Model of MSTTE

The MSTTE loop was modeled in SAM primarily using *PBPipe* components to capture the loop piping, which models 1-D fluid flow with conjugate heat transfer to a cylindrical-geometry *HeatStructure* pipe wall (see Table 8 and Figure 23) [22]. The HIS is also modeled using a *PBPipe* for the shell-side portion of the flow and a *PBCoupledHeatStructure* to represent the injection tubes. However, the present model directly specifies a tritium injection rate as a volumetric source term in the HIS fluid region. Future work will identify appropriate closure correlations for the inline square bundle geometry so that tritium injection can be modeled based on pressure in the injection tubes. The Gnielinski correlation [22] is used to calculate the heat transfer coefficient in all *PBPipe* components, which is then used to determine the mass transfer coefficient via the Chilton-Colburn analogy. The fluid volumes in the experiment loop plenum and the salt tank in the Copenhagen Atomics test stand are captured using 0-D *PBLiquidVolume* and *PBVolumeBranch* components, and the pump is modeled using a *PBPump* component.

Table 8. MSTTE facility SAM model parameters and operating/boundary conditions.

Fluid material properties	FLiBe	Tritium injection rate (mol/s)	1.0×10^{-10}
Solid material properties	316 SS	Outer wall surface temp. BC	Adiabatic
Axial element size (mm)	~ 50	Outer wall surface tritium BC	Adiabatic
Radial wall element size (mm)	0.33	Outer wall test section tritium BC	$c_{surf} = 0.0$
Baseline flow rate (LPM)	100	Baseline temperature (°C)	600

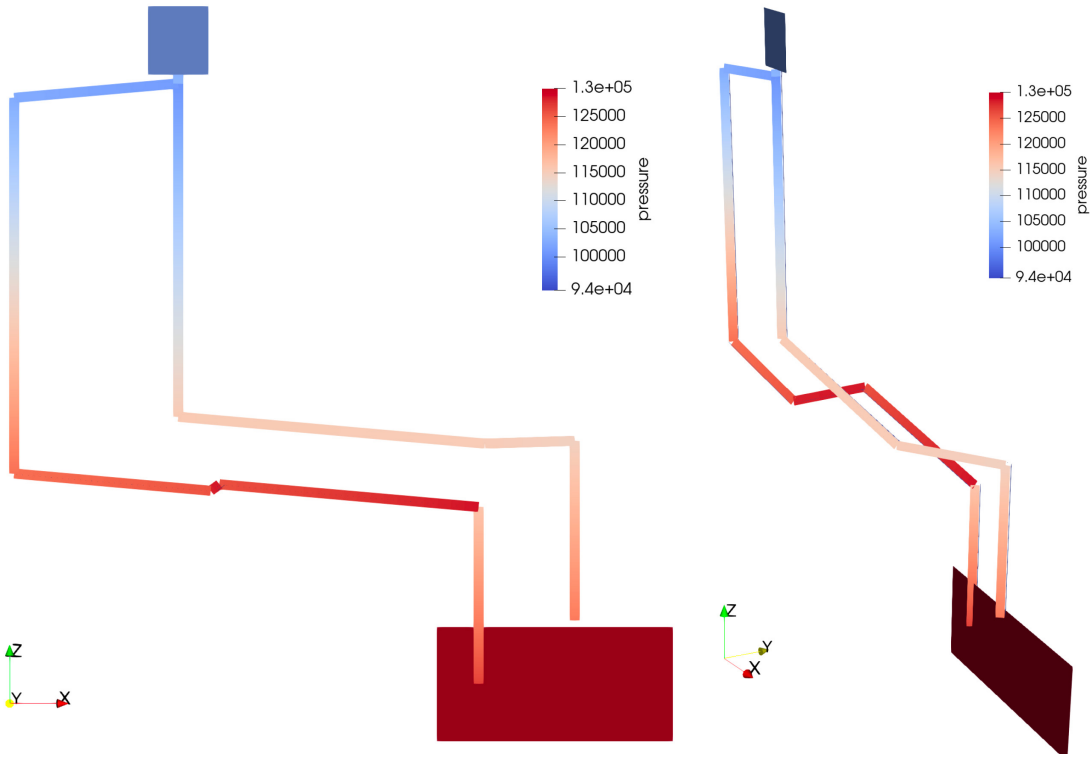

Figure 23. SAM model of the MSTTE facility with predicted fluid pressure distributions (Pa) at nominal conditions with profile (left) and skewed (right) point of views.

The focus of this initial modeling effort is to demonstrate a coupled thermal hydraulics and tritium transport simulation of the MSTTE facility, capturing the geometry with reasonable fidelity and accuracy. Assuming that there is sufficient trace heating applied to the loop, the outer piping surface is assumed to be adiabatic and heat loss is neglected. This assumption is also applied to tritium transport in the current model, such that tritium only permeates through the outer wall surface in the test section, where the concentration is assumed to be zero at the vacuum-facing surface. Although an empirical convective evolution model at gas-liquid interface is available in the SAM tritium transport model, it is not exercised in the current analysis. In the baseline study, the loop is operated at 600°C with 100 LPM flow with a nominal tritium injection rate in the HIS that is assumed to be constant at 1.0×10^{-10} mol/s for three days, followed by a higher injection rate of 2.0×10^{-10} mol/s held for an additional four days. Initial injection rates of 1.0×10^{-11} and 1.0×10^{-9} mol/s were also simulated at the baseline flow conditions and are shown in Figure 24. Overall, it was observed that it takes approximately ~2 days for the permeation of tritium through the outer wall of the test section to reach a steady state balancing the prescribed injection rate. At nominal conditions, the average concentration of T_2 in the test section is on the order of 10^{-5} mol/m^3. Note that the injection rate largely did not impact the transient aspects of tritium transport, with the average concentration and permeation rates scaling directly with the injection rate.

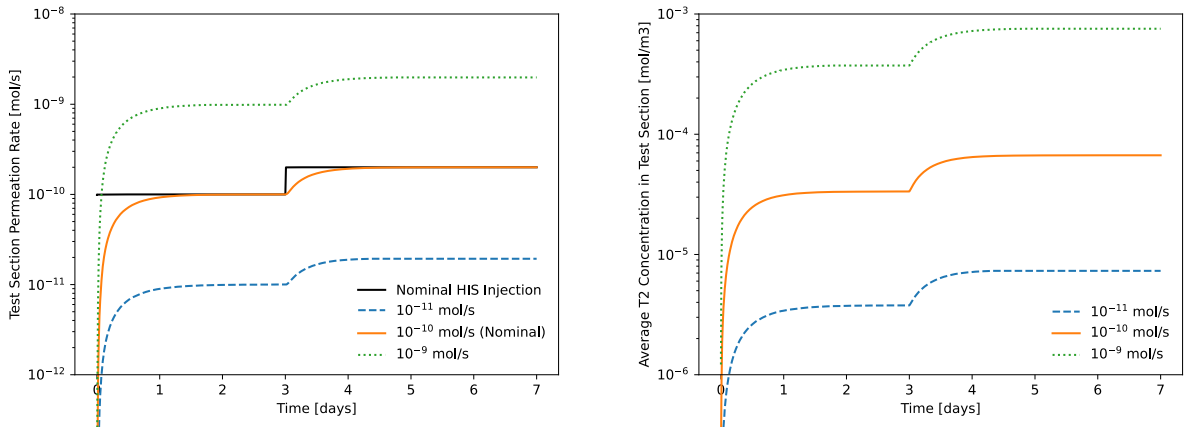

Figure 24. Tritium permeation rates through the test section outer wall (left) and the average T_2 concentrations in the test section (right) under nominal flow at different injection rates.

3.4 Parametric Study of Predicted Permeation Rates

A parametric study of the impact of flow conditions in the loop on the tritium transport behavior was performed within some general bounds of the anticipated operating conditions between 550–650°C with flow rates of 50–100 LPM at the nominal tritium injection rate described in the previous section. Overall, it was observed that both flow and temperature did affect the time it took for the permeation through the test section to reach an equilibrium with the injection rate, where higher flow rates and/or higher operating temperatures resulted in shorter times to equilibrium as shown in Figure 25. This corresponds also to the average T_2 concentration in the test section and loop, as a slower time to equilibrium resulted in more tritium being injected and held up in the system before removal through permeation as shown in Figure 26.

The transport mechanism under these conditions is largely mass-transfer limited, therefore the operating parameters that directly impact the convective mass transfer rate correlate to the observed transport behavior. Lower temperatures and flow rates (fluid velocities) result in smaller calculated heat and mass transfer coefficients and thus lower mass transfer rates from the bulk FLiBe to and permeating through the 316 SS tubing walls as summarized in Table 9. A steady-state extraction efficiency (net normalized concentration of T_2) is quickly established, although the average concentrations in the test section will continue to rise until an equilibrium is reached. It is observed that the extraction efficiency is primarily dependent on the permeability of the tubing wall, with greater impact from the operating temperature than from the flow rate.

The present analysis demonstrates the tritium transport modeling capability in SAM as applied to the MSTTE facility, including the impacts of the direct coupling with thermal hydraulic simulation. Future work will investigate the impact of injection by permeation through the HIS injection tubes, evaporation in the plenum, tritium leakage through the non-test section loop piping, as well as tritium leakage and/or heat loss through the test section outer vacuum shell wall.

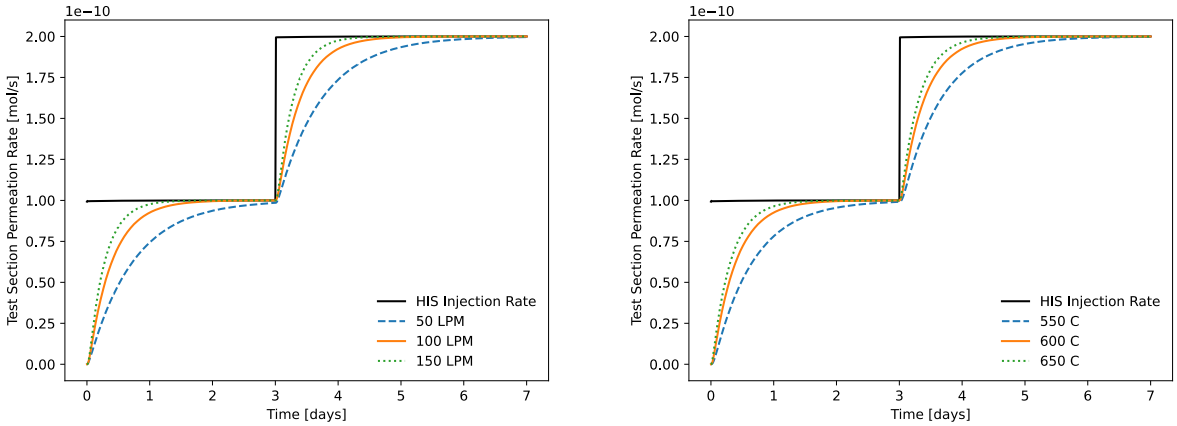

Figure 25. Tritium permeation rates through the test section outer wall for different flow rates at 600°C temperature (left) and for different temperatures at 100 LPM flow (right).

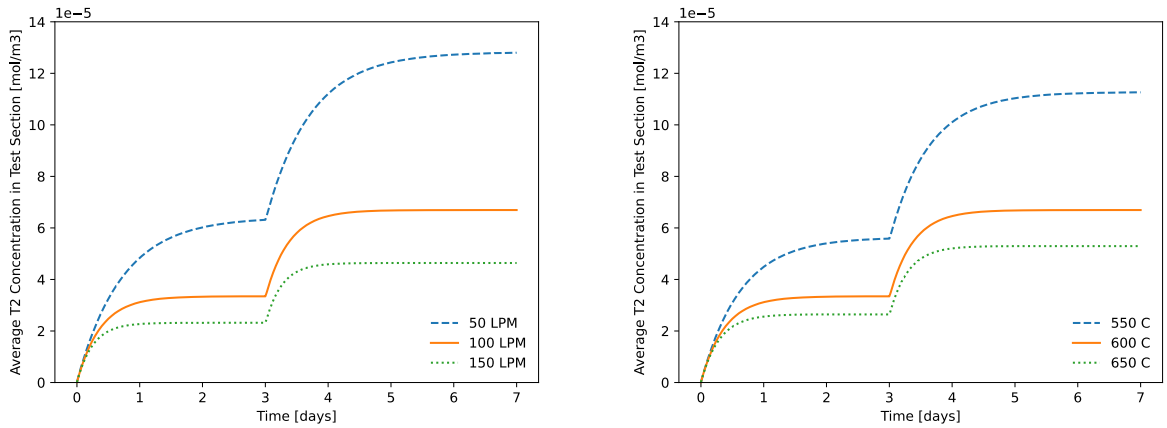

Figure 26. Average T_2 concentrations in the test section for different flow rates at 600°C temperature (left) and for different temperatures at 100 LPM flow (right).

Table 9. Predicted mass transfer coefficients, permeability, and average extraction efficiency ($[T_{2,in} - T_{2,out}] / T_{2,in}$) of the MSTTE test section under different flow conditions.

Flow rate (LPM)	Temperature (°C)	Mass Transfer Coeff. (mm s^{-1})	Permeability (mol m^{-1} s^{-1} $Pa^{-0.5}$)	Extraction Efficiency (%)
50	600	0.0312	3.17×10^{-11}	0.18
100	600	0.0598	3.17×10^{-11}	0.17
150	600	0.0863	3.17×10^{-11}	0.16
100	550	0.0355	1.90×10^{-11}	0.12
100	600	0.0598	3.17×10^{-11}	0.17
100	650	0.0756	5.03×10^{-11}	0.24

4. MSTTE TEST SECTION CFD

The primary aim of this section is to analyze the fluid flow in the permeation test section to ensure fully developed flow is achieved prior to the entrance of the measurement zone. The challenge is to meet experiment size constraints, pressure drop requirements, and maintian sufficient surface area in the test section to measure permeation rates. The correlation between entrance length (L_e, m), pipe inner diameter (D, m), and Reynolds Number (Re, dimensionless) in the turbulent flow regime is:

$$L_e = 4.4D(Re)^{1/6} \tag{7}$$

With the required entrance length plotted as a function of flow rate in Figure 27. The entrance length is greater than the current design specificaiton. Although the entrance length correlation is for a fluid entering a pipe and not for the developing flow length after a pipe bend, the entrance length correlation is commonly used as an approximation.

The focus of this section is to use Computational Fluid Dynamics (CFD) models to ensure that the salt flow is in a fully developed state upon entering a designated test section for permeation measurements by assesing design changes. The CFD analysis encompasses a single-phase simulation involving the vertical upward flow of FLiNaK under conditions of thermal isothermality. Turbulent flow conditions were examined using 100 LPM of salt flow as a design basis with the dimensions from Figure 11.

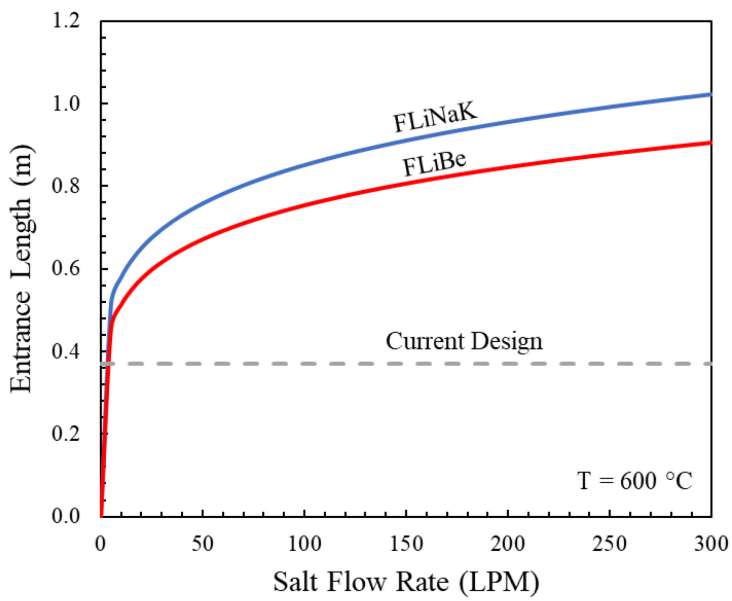

Figure 27. Entrance length versus salt flow rate for FLiNaK and FLiBe at 600 °C using current design specifications.

4.1 Turbulence Modeling

A CFD model was developed for the MSTTE permeator using ANSYS Fluent 19.2V. The standard k-epsilon turbulence model is adopted for the present study, with other models applied for comparison. Standard k-epsilon offers a good compromise between numerical effort and computational accuracy. However, when presented with flow perturbations like flow separation, moderate swirl and secondary flow behavior may not be fully resolved. Thus, realizable k-epsilon was utilized in comparison with standard k-epsilon since this two-equation model can resolve any swirl flow caused by separation. See Appendix C for a comparison table on turbulence models. The general form of standard k-epsilon turbulent in the x-direction (this applies to the y-and-z-direction) is as follows:

$$\frac{\partial(\rho k)}{\partial t}+\frac{\partial}{\partial x_j}\cdot(\rho u_j k)=\frac{\partial}{\partial x_j}\cdot\left[\left(\mu+\frac{\mu_t}{\sigma_k}\frac{\partial}{\partial x_j}k\right)\right]+p_k+p_b-\rho\varepsilon \tag{8}$$

$$\frac{\partial(\rho\varepsilon)}{\partial t}+\frac{\partial}{\partial x_j}\cdot(\rho u_j \varepsilon)=\frac{\partial}{\partial x_j}\cdot\left[\left(\mu+\frac{\mu_t}{\sigma_\varepsilon}\frac{\partial}{\partial x}\varepsilon\right)\right]+C_{1\varepsilon}\frac{\varepsilon}{k}\ (p_k+C_3p_b)-C_2\rho\frac{\varepsilon^2}{k} \tag{9}$$

Where k, ε, and μ_t are the kinetic energy, dissipation, and turbulent viscosity.

$$\mu_t=\rho C_\mu\frac{k^2}{\varepsilon} \tag{10}$$

Then p_k and p_b as the kinetic energy generation due to mean velocity gradients and buoyancy, respectively.

$$p_k=-\rho\overline{u_i'u_j'}\ \frac{\partial u_j}{\partial x_i}\ ;p_k=\beta g_i\frac{\mu_t}{Pr_t}\frac{\partial T}{\partial x_i};\ \beta=-\frac{1}{\rho}\left(\frac{\partial\rho}{\partial T}\right)_p \tag{11}$$

Where, Pr_t is the Prantdl number and g_i is the gravitational vector component in the ith direction. While $C_{1\varepsilon}$, C_2, C_3, C_μ , σ_k, and σ_b are constants:

$$C_{1\varepsilon}=1.44\,,C_2=1.92\,,C_3=0,C_\mu=0.09,\sigma_k=1.0,\sigma_\varepsilon=1.3$$

Whereas the realizable k-epsilon turbulent model is as follows:

$$\frac{\partial(\rho k)}{\partial t}+\frac{\partial}{\partial x_j}\cdot(\rho u_j k)=\frac{\partial}{\partial x_j}\cdot\left[\left(\mu+\frac{\mu_t}{\sigma_k}\frac{\partial}{\partial x_j}k\right)\right]+p_k+p_b-\rho\varepsilon-Y_M \tag{12}$$

$$\frac{\partial(\rho\varepsilon)}{\partial t}+\frac{\partial}{\partial x_j}\cdot(\rho u_j \varepsilon)=\frac{\partial}{\partial x_j}\cdot\left[\left(\mu+\frac{\mu_t}{\sigma_\varepsilon}\frac{\partial}{\partial x_j}\varepsilon\right)\right]+\rho C_1S\varepsilon-\ \rho C_2\frac{\varepsilon^2}{k+\sqrt{v\varepsilon}}\ +C_{1\varepsilon}\rho\frac{\varepsilon}{k}\tanh\left|\frac{v}{u}\right|p_b \tag{13}$$

$$C_1=\max\,[0.43,\frac{\acute{\eta}}{\acute{\eta}+5},\acute{\eta}=S\frac{k}{\varepsilon},S=\sqrt{2S_{i,j}S_{i,j}} \tag{14}$$

$$\mu_t=\rho C_\mu\frac{k^2}{\varepsilon}\quad,C_\mu=\frac{1}{A_0+A_s\frac{kU^*}{\varepsilon}}\ ,U^*=\sqrt{S_{i,j}S_{i,j}+\widetilde{\Omega_{i,j}}\widetilde{\Omega_{i,j}}} \tag{15}$$

$$\widetilde{\Omega_{i,j}}=\Omega_{i,j}-2\varepsilon_{i,j,k}\omega_k\ ,\qquad \Omega_{i,j}=\overline{\Omega_{i,j}}-2\varepsilon_{i,j,k}\omega_k \tag{16}$$

Where $\overline{\Omega_{i,j}}$ is the mean rate-of-rotation tensor viewed in a moving reference frame with the angular velocity ω_k. Then p_k and p_b as the kinetic energy generation due to mean velocity gradients and buoyancy, respectively. While $C_{1\varepsilon}$, C_2, σ_k, σ_b , A_0 , and $A_s$are constants:

$$C_{1\varepsilon}=1.44\,,C_2=1.9\,,\sigma_k=1.0,\sigma_\varepsilon=1.2\,,A_0=4.04;\ A_s=\sqrt{6}\cos(\varphi)$$

$$\varphi=\frac{1}{3}cos^{-1}(\sqrt{6}W),W=\frac{S_{i,j}S_{j,k}S_{k,i}}{\widetilde{S^3}},\tilde{S}=\sqrt{S_{i,j}S_{i,j}},S_{i,j}=\frac{1}{2}(\frac{\partial u_j}{\partial x_i}+\frac{\partial u_i}{\partial x_j}) \tag{17}$$

The main difference between the standard and realizable models is the treatment of turbulent viscosity with the first being constant and the latter being non-linear. In the context of turbulent flows, the procedure of mesh generation within the fluid domain assumes a significant role in CFD modeling due to the imposition of y-plus criteria by specific two-equation turbulence model near wall treatment. The y-plus parameter, a dimensionless quantity, characterizes the spatial distance from the wall to the central point of the first grid cell. The mesh generated for the MSTTE permeator is composed of hexahedron elements with an increasing bias in the proximity of the walls (Figure 28).

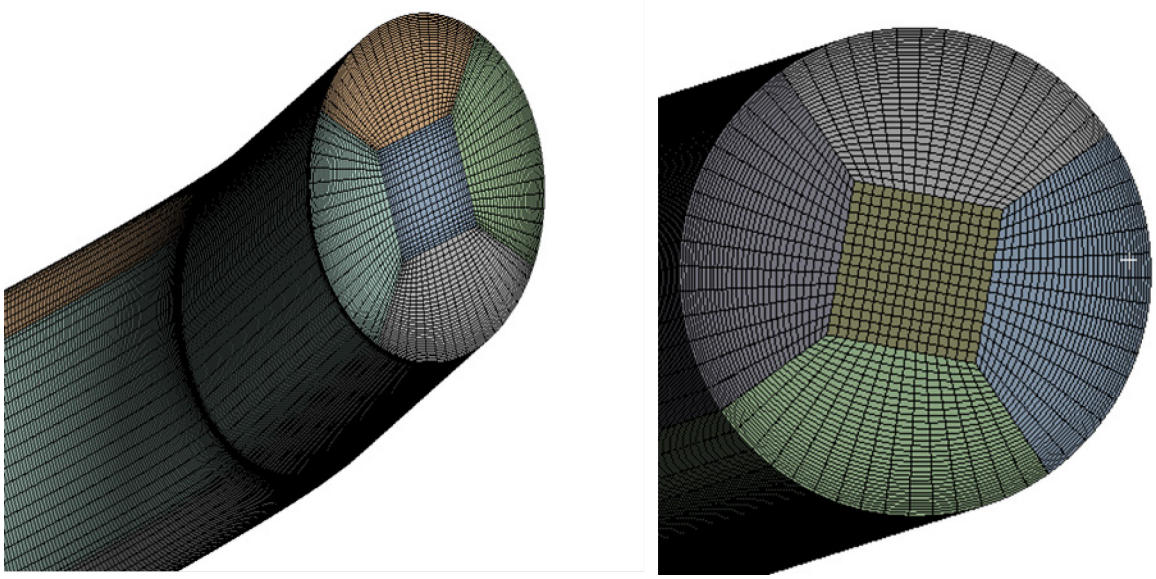

Figure 28. Mesh grid for top and bottom bend of MSTTE external test section (left). Mesh grid for the permeator test section (right).

Table 10 describes the physical properties and geometrical information of the MSTTE permeator test section CFD model.

Table 10. Geometrical and physical properties of fluid and MSTTE permeator, respectively.

Pipe Diameter [m] (OD)	3.81×10^{-2}
Pipe Wall Thickness [m] (WT)	1.65×10^{-3}
Pipe Diameter [m] (ID) (OD-WT)	3.65×10^{-2}
Pipe Radius [m]	1.82×10^{-2}
Pipe Area [m^2]	1.04×10^{-3}
Liquid Velocity [m/s] (Turbulent)	1.60×10^{0}
FLiNaK Density [kg/m3]	2.03×10^{3}
FLiNaK Viscosity [kg/m-s]	4.20×10^{-3}
RE Turbulent	2.82×10^{4}

4.2 Overview of CFD Results

Pipe bends result in flow separation and the subsequent manifestation of secondary-swirling behavior. Figure 29 depicts the secondary flow phenomenon with the normalized velocity vector field for a flow in the MSTTE external test section 85º bend. Swirling behavior is also predicted due to the detached of the secondary flow as shown in Figure 30.

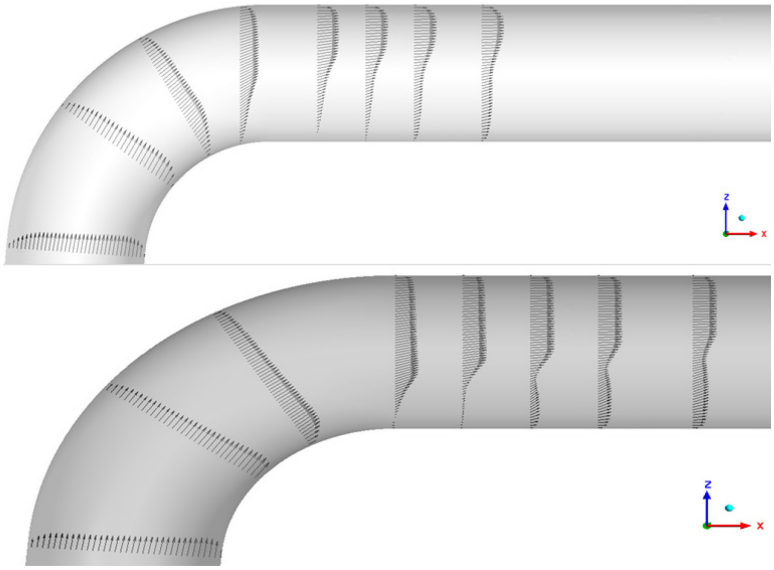

Figure 29. Normalized velocity vector field for 10 LPM (top) and 100 LPM (bottom).

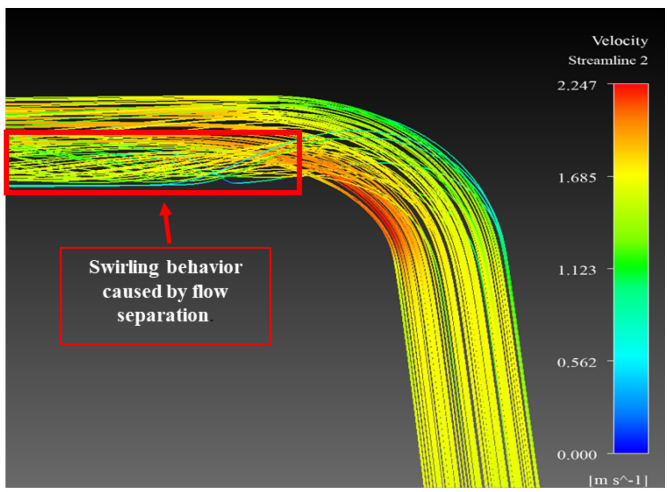

Figure 30. Streamlines visualizing the swirling effect caused by the flow separation in the 85° bend.

In the pursuit of achieving numerical precision in the representation of turbulent phenomena, an assessment was undertaken regarding the y-plus values. Simulations revealed instances wherein the y-plus values deviated below prescribed criteria due to the separation of bodies in the overall domain. Consequently, an iteration involving domain refinement was executed to rectify this discrepancy. After an in-depth inquiry, it became evident that the refinement increased in the y-plus values but severely increased the computational time, thereby necessitating the adoption of Scalable Wall Treatment. The Standard Wall Treatment was also employed for comparison between the near wall treatments. If the Scalable and Standard wall treatment match in velocity profile, then the mesh is sufficient for turbulent and wall treatment model.

Due to computational expense a mesh independence study was not conducted in most cases. Instead, the highest reasonable mesh was utilized in the finalization of these results. For more information on CFD mesh information refer to Appendix C.

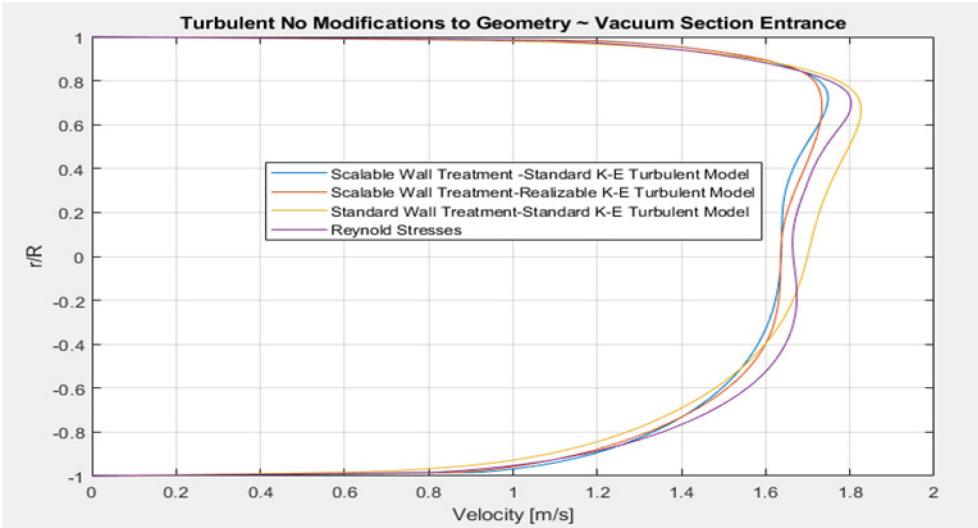

Figure 31. Velocity profiles for turbulent 100 LPM case.

Figure 31 shows the velocity profile at the anticipated entrance location of the permeator in the current design. These results indicate that the flow is in the developing regime. The inability to reach fully developed flow is a result of insufficient pipe length and swirl effects from the flow separation in the bend. The following sections investigate options to achieve fully developed flow while addressing design constraint of overall length.

4.3 Analysis of Reducers

Reducers decrease the hydraulic diameter thus decreasing the required developing flow length. Concentric and eccentric reducers are investigated for effects on flow behavior. The reducers and expanders were placed before and after the bends. The outlet diameter of the reducers investigated were 0.5 in. and 1 in. with a visual representation in Figure 32.

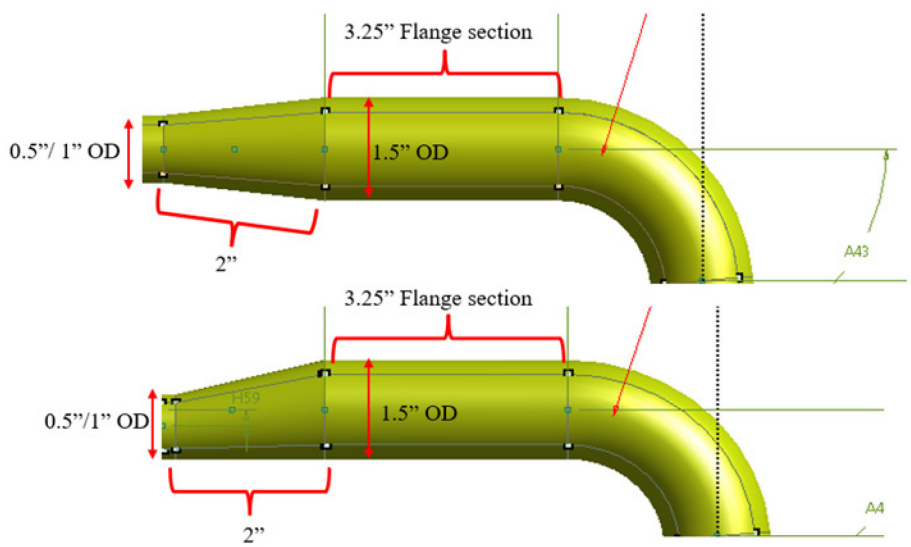

Figure 32. Geometrical representation of the concentric (top) and eccentric (bottom) reducers.

Figure 33. Eccentric (top) and reversed eccentric (bottom) reducer geometries.

Provided that the swirl phenomena occur at the bend and extends asymmetrically ~45° from the centerline, the eccentric reducer was rotated 180° for comparison with a non-rotated eccentric reducer. The identification of this rotation is labeled as "Reversed Eccentric" and is visualized in Figure 33. As elucidated within the turbulent segment of this report, the complexity of turbulence mandates the utilization of an elevated radial mesh. Accordingly, a mesh composed of hexahedron elements characterized by an augmentation in cell count in proximity to the reducer wall was employed. A visual depiction of this arrangement is presented in Figure 34.

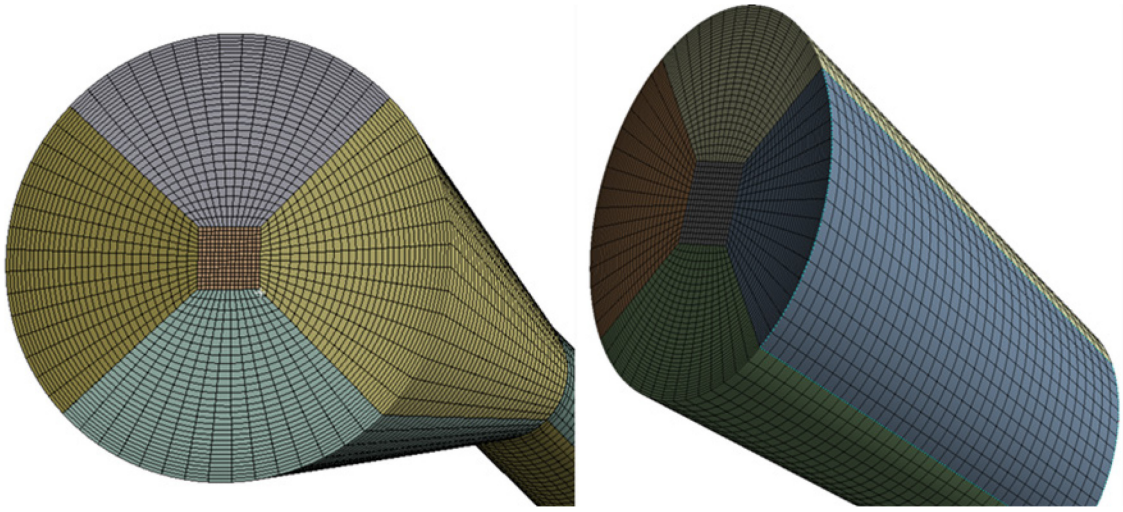

Figure 34. Mesh used for concentric (left) and eccentric (right) reducers.

4.3.1 Concentric Reducer/Expander CFD Results

In this section, the velocity profile at the entrance of the test section vacuum boundary are shown for the concentric reducers with reduced ODs of 1 in. (Figure 35) and 0.5 in. (Figure 36). If a near symmetrical velocity profile occurred at the vaccum section, then mutltiple profiles at different location were analyzed (Figure 37).

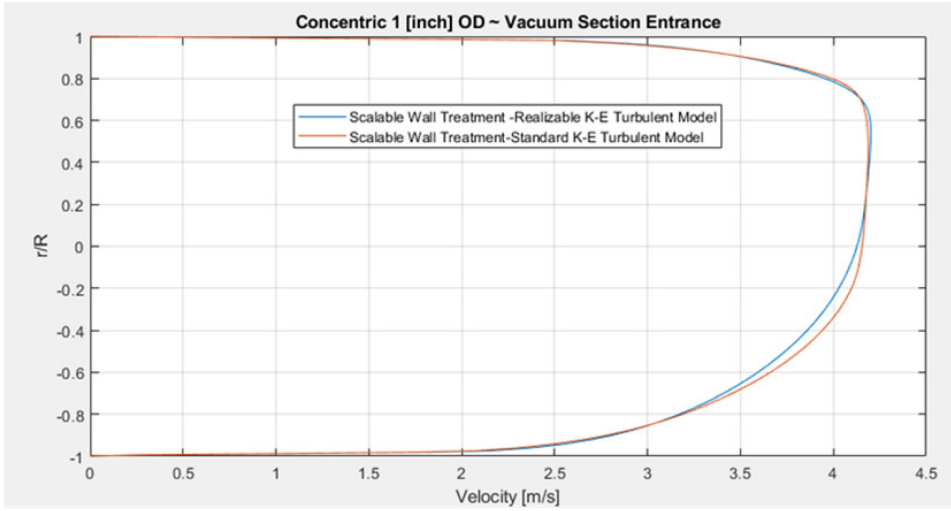

Figure 35. Velocity profiles at the test section vacuum boundary entrance for the 1 inch concentric reducers.

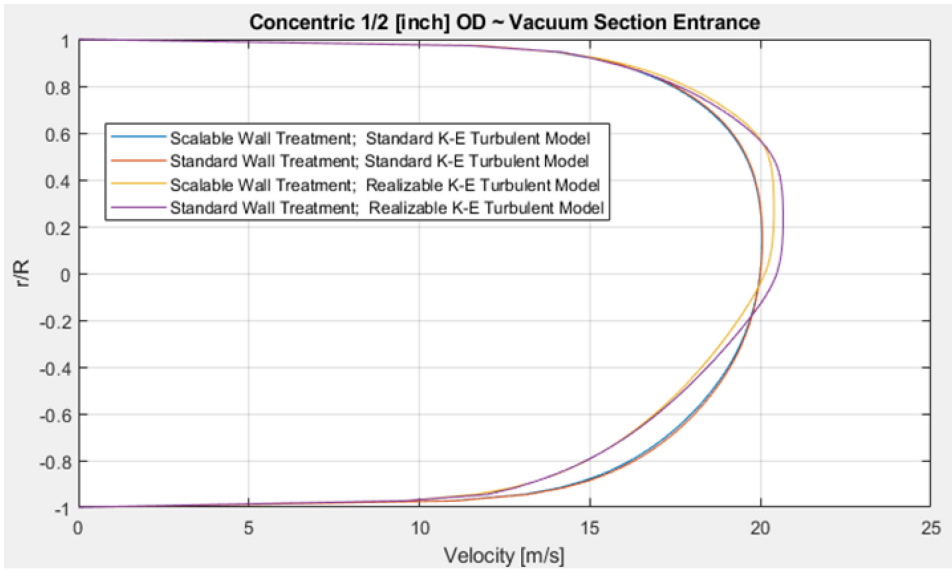

Figure 36. Velocity profiles at the test section vacuum boundary entrance for the 0.5 inch concentric reducers.

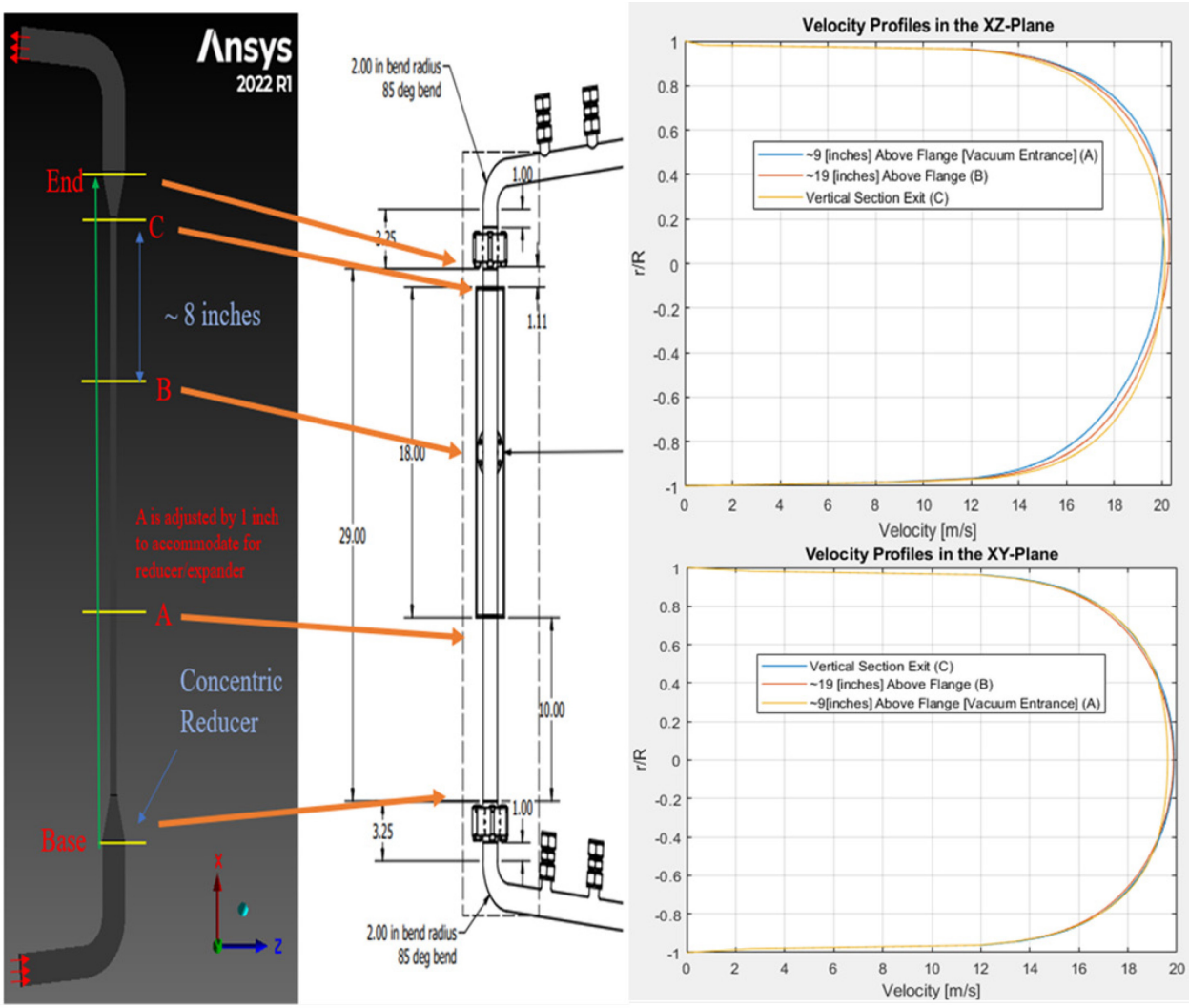

Figure 37. The location identification for the 0.5 in. concentric reducers velocity profiles (left); velocity profiles in the XZ-Plane (top-right) and XY-Plane (bottom-right).

The simulation for the 0.5 in. reducer predicts symmetric and near fully developed profile. These results were taken from a standard k-epsilon turbulence model with standard wall treatment (see Appendix C for mesh metrics). In the interest of comparison, different turbulent and wall treatment models were applied to the 0.5 in. concentric reducer with the results shown in Figure 37. Herein, it shows the 0.5-in. reducer results in a fully developed flow profile.

4.3.2 Eccentric Reducer/Expander CFD Results

In this section the velocity profiles, taken at the anticipated vacuum section entrance, are shown for the eccentric reducers at two different reductions ODs of 1 in. (Figure 38) and 0.5 in. (Figure 39). If a near symmetrical velocity profile occurred at the vaccum section then mutltiple profiles at different location were analyzed (Figure 40).

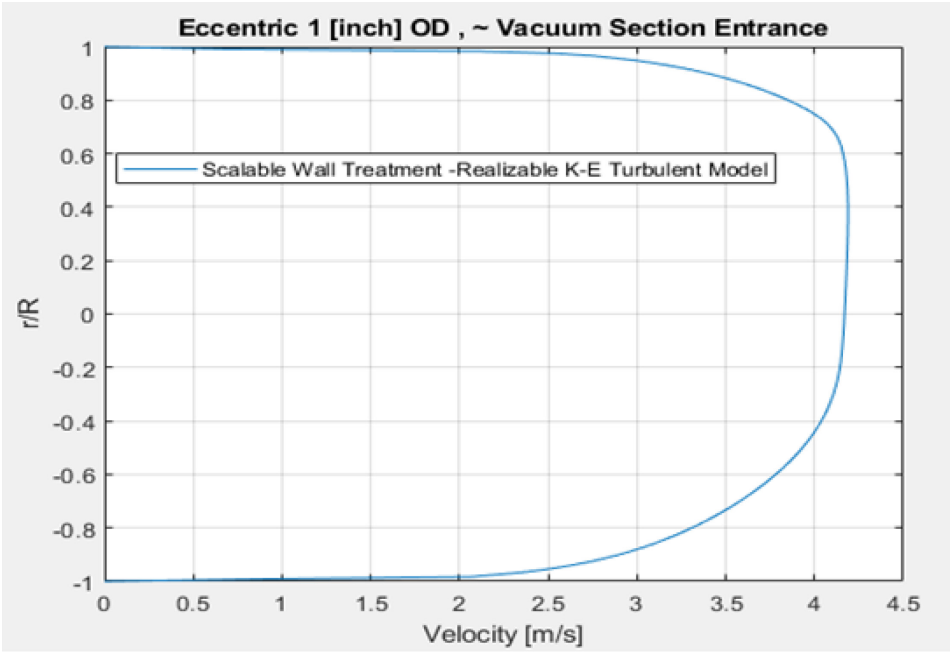

Figure 38. Velocity profile at the test section vacuum boundary entrance for 1-in. concentric reducer.

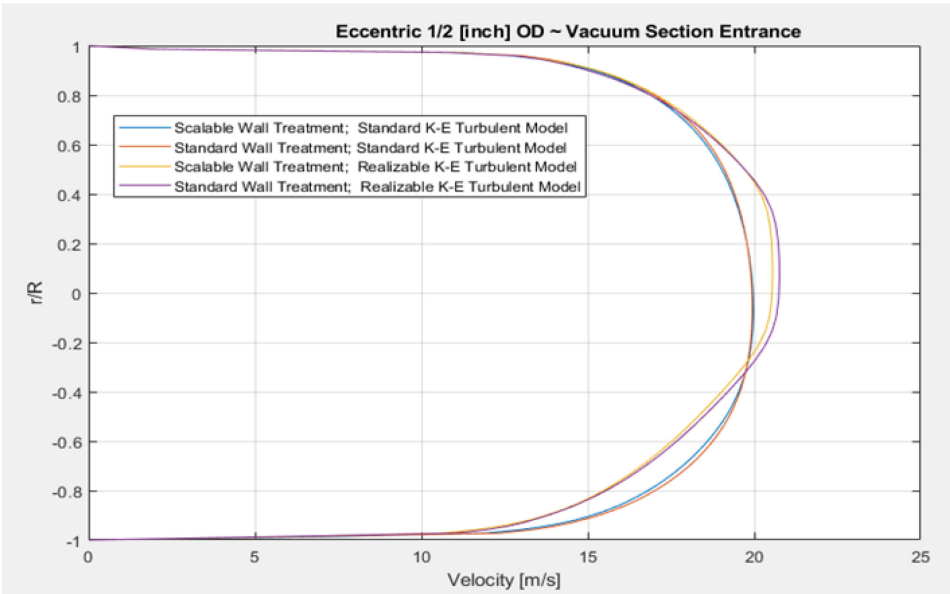

Figure 39. Velocity profile at the test section vacuum boundary entrance for 0.5-in. eccentric reducer.

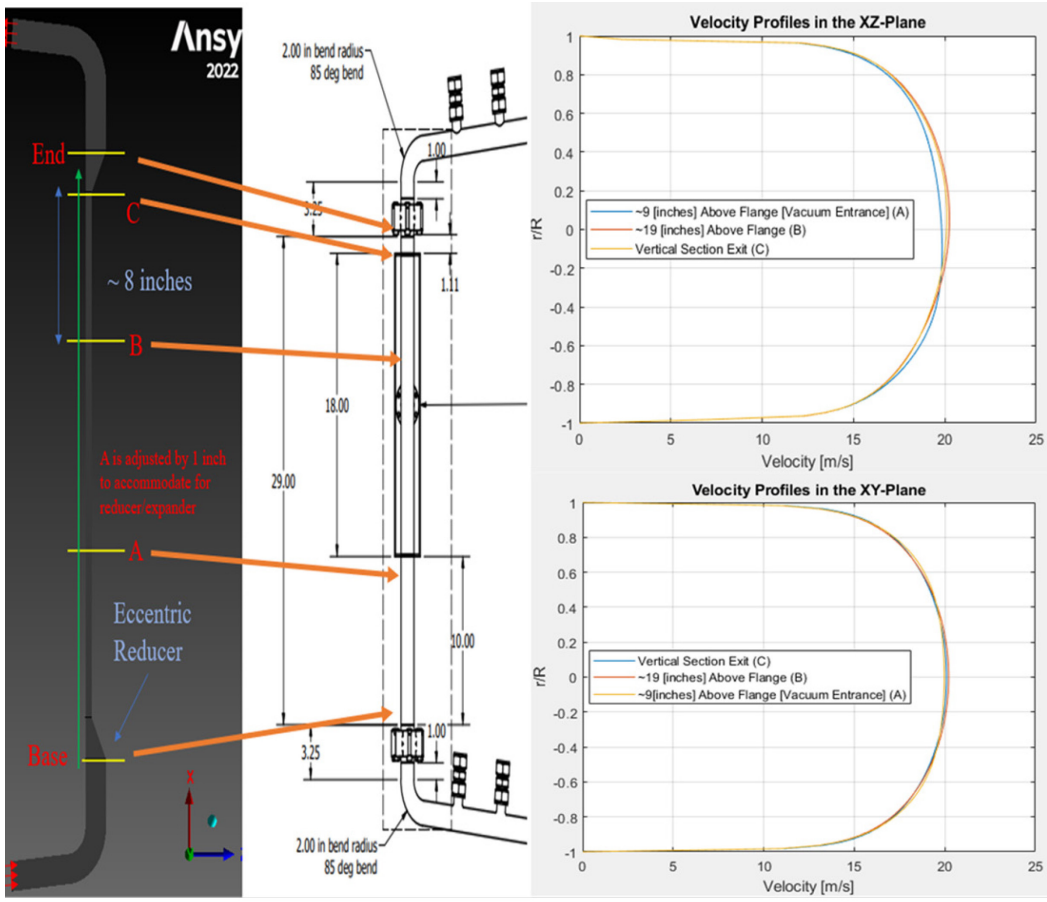

Figure 40. The location identification for the 0.5-in eccentric reducers velocity profiles (left); velocity profiles in the XZ-Plane (top-right) and XY-Plane (bottom-right).

4.3.3 Reversed Eccentric Reducer/Expander

The velocity profiles taken at the anticipated vacuum section entrance are shown for the reversed eccentric reducers at two different reductions of 1 inch (Figure 41) and 0.5 inch (Figure 42). Velocity profiles at multiple locations are reported in Figure 43 for the 0.5 inch reversed eccentric reducers configuration.

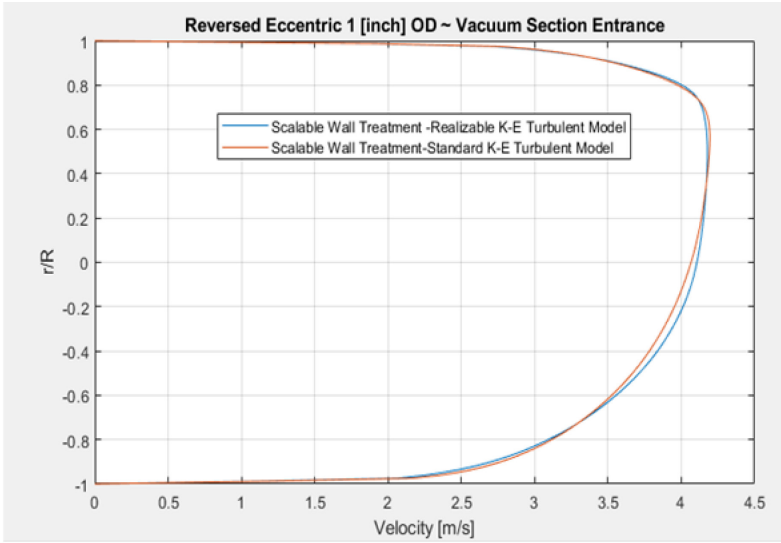

Figure 41. Velocity profiles at the test section vacuum boundary entrance for 1 inch reversed eccentric reducer.

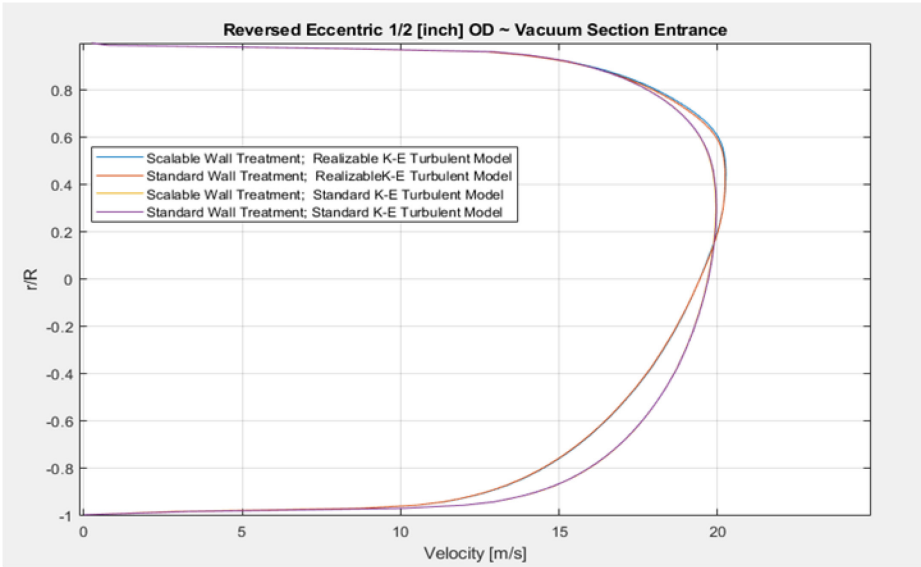

Figure 42. Velocity profiles at the test section vacuum boundary entrance for 0.5 inch reversed eccentric reducer.

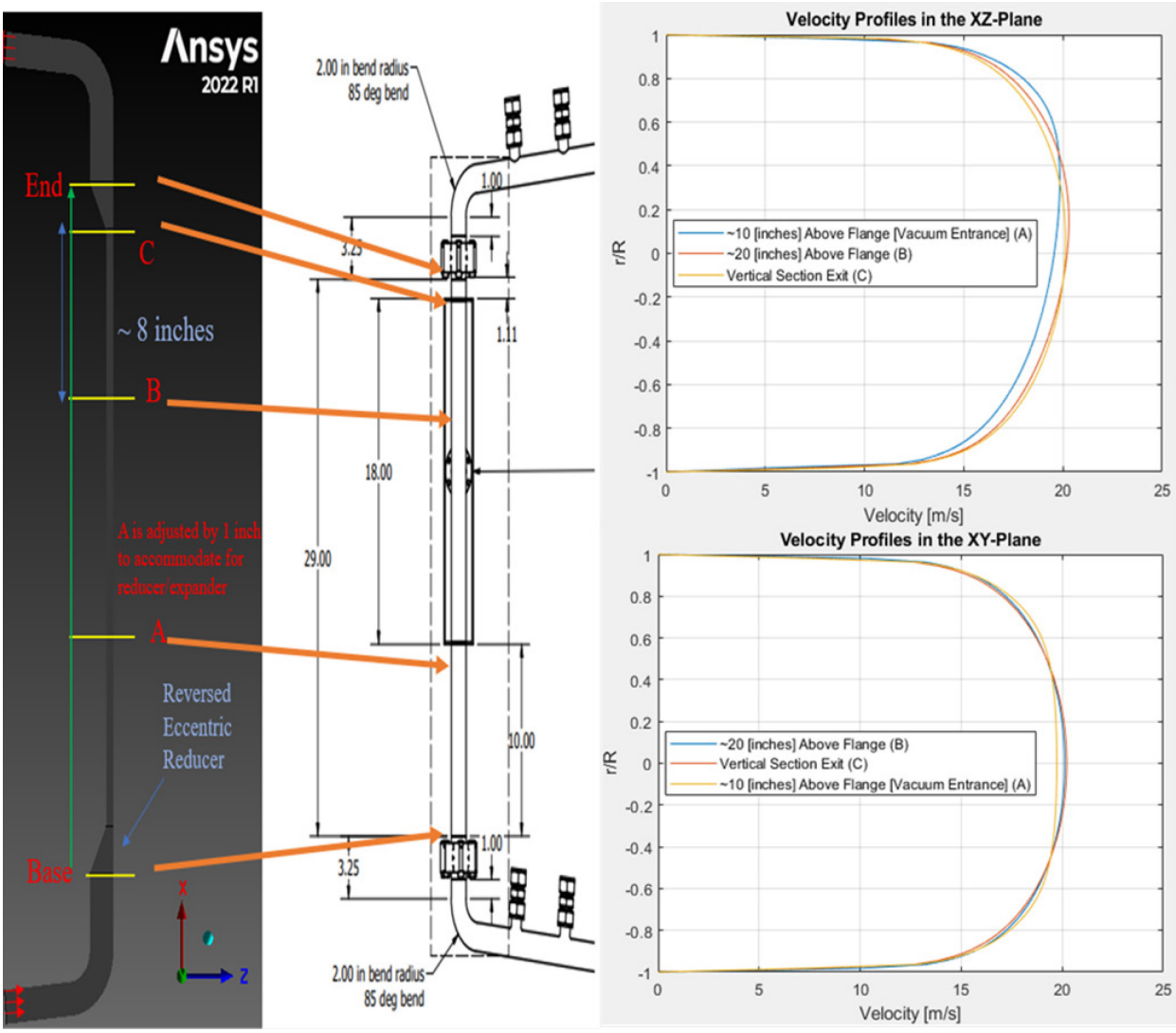

Figure 43. The location identification for the 0.5 inch reversed eccentric reducers velocity profiles (left); velocity profiles in the XZ-Plane (top-right) and XY-Plane (bottom-right).

4.4 Analysis of Flow Conditioners

CFD models of Flow Conditioners (FC) were performed as an alternative concept to reducers. FCs enhance the precision of flow rate measurements after certain flow perturbations such as bends. These devices serve to rectify the flow profile by inducing controlled interaction between a highly swirling stream and a less swirling counterpart. Subsequently, the compressed flow in the FC increases the viscous sublayer relative to a non-confined flow, further reducing eddies that contribute to turbulence. Although an FC can reduce highly swirling streams it is not a guarantee that a fully developed profile will be achieved at a needed position.

Among the numerous available design configurations, the selection was confined to the Laws and NEL configurations. It should be noted that a comprehensive design and sensitivity analysis is imperative to encompass the utility and effectiveness of an FC. This sensitivity analysis would consist of but not limited to turbulence models, hole diameter, number of holes, positioning of an FC, and hole placement.

In literature, investigators arbitrarily design their flow conditioner with no basis other than the configurations in terms of achieving fully developed velocity profile at a needed position. Instead, many are designed based off pressure drop and porosity with some consideration in corrosion. Thus, the design of a flow conditioner for the purpose of flow development is a trial-and-error method. However, an investigator's design can be used as a template with modification of flow conditioner holes to fit the pipe. Figures 44 and 45 are snapshots of the preliminary flow conditioner designs.

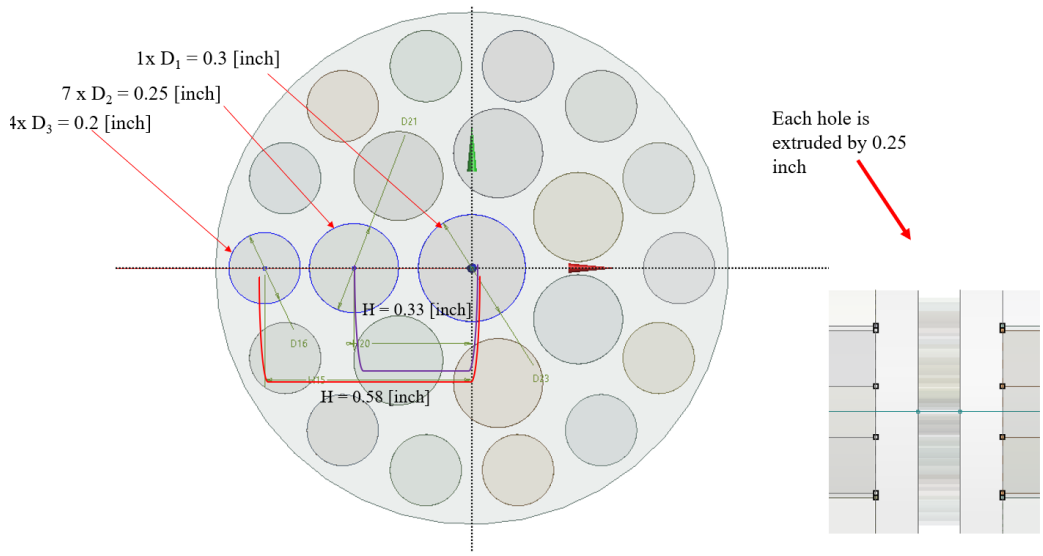

Figure 44. Laws flow conditioner design.

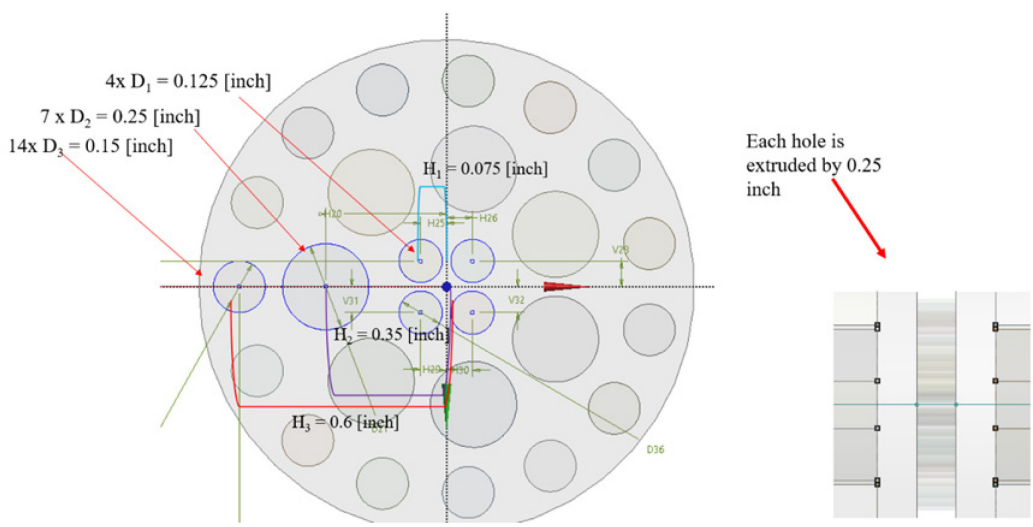

Figure 45. NEL flow conditioner design.

The purpose of the flow conditioner is to straighten the swirling streams caused by the flow separation in the 85° bend. Figure 46 shows the results when adding a Laws flow conditioner to the MSTTE Permeator. In the top image, the flow conditioner corrects the swirling behavior, as intended, caused by the flow separation in the bend. The results in Figure 46 depict symmetric and near fully developed profile. These results were taken from a realizable k-epsilon turbulence model with Scalable Wall treatment, see Appendix C for mesh metrics.

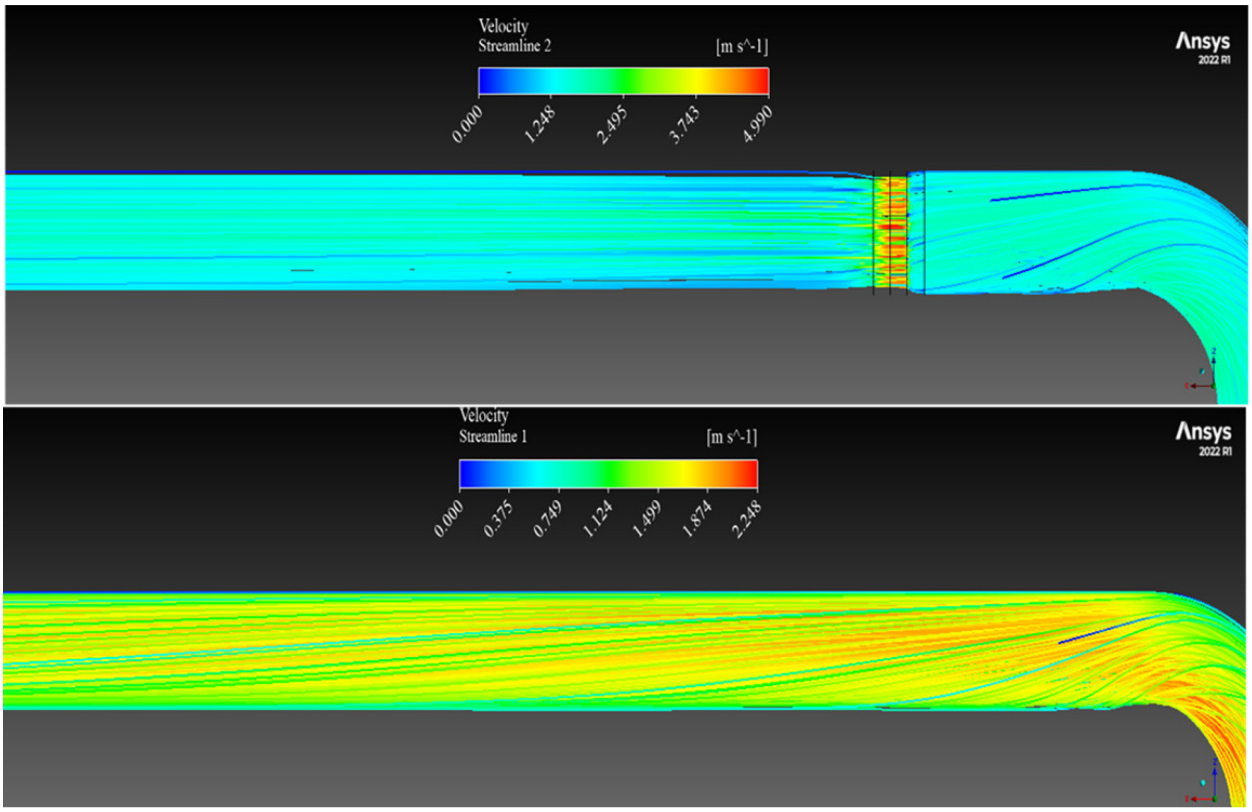

Figure 46. Streamlines with Laws type flow conditioner (top) and without conditioner (bottom).

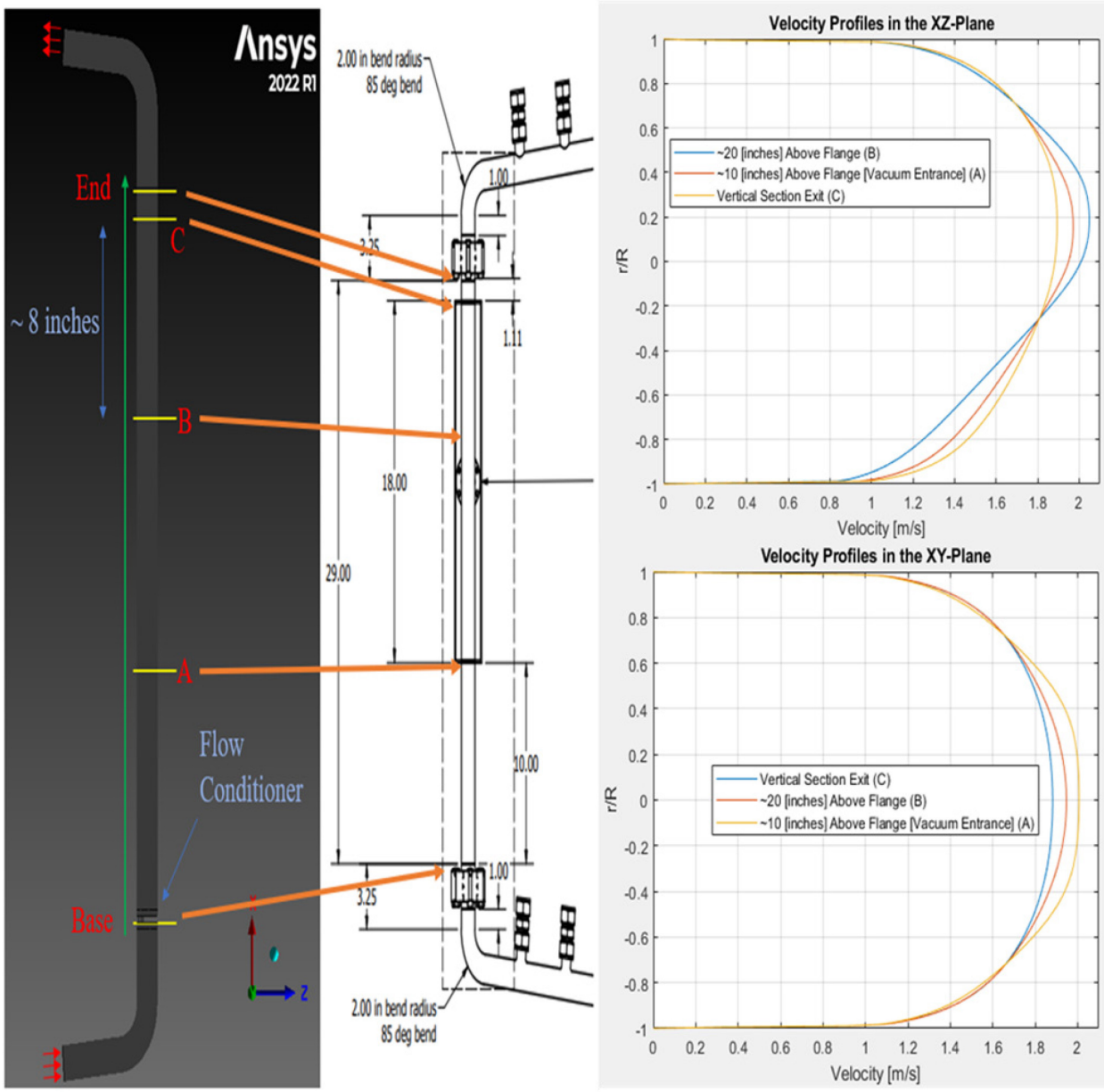

Figure 47. The location identification for the Laws design flow conditioner (left); velocity profiles in the XZ-Plane (top-right) and XY-Plane (bottom-right).

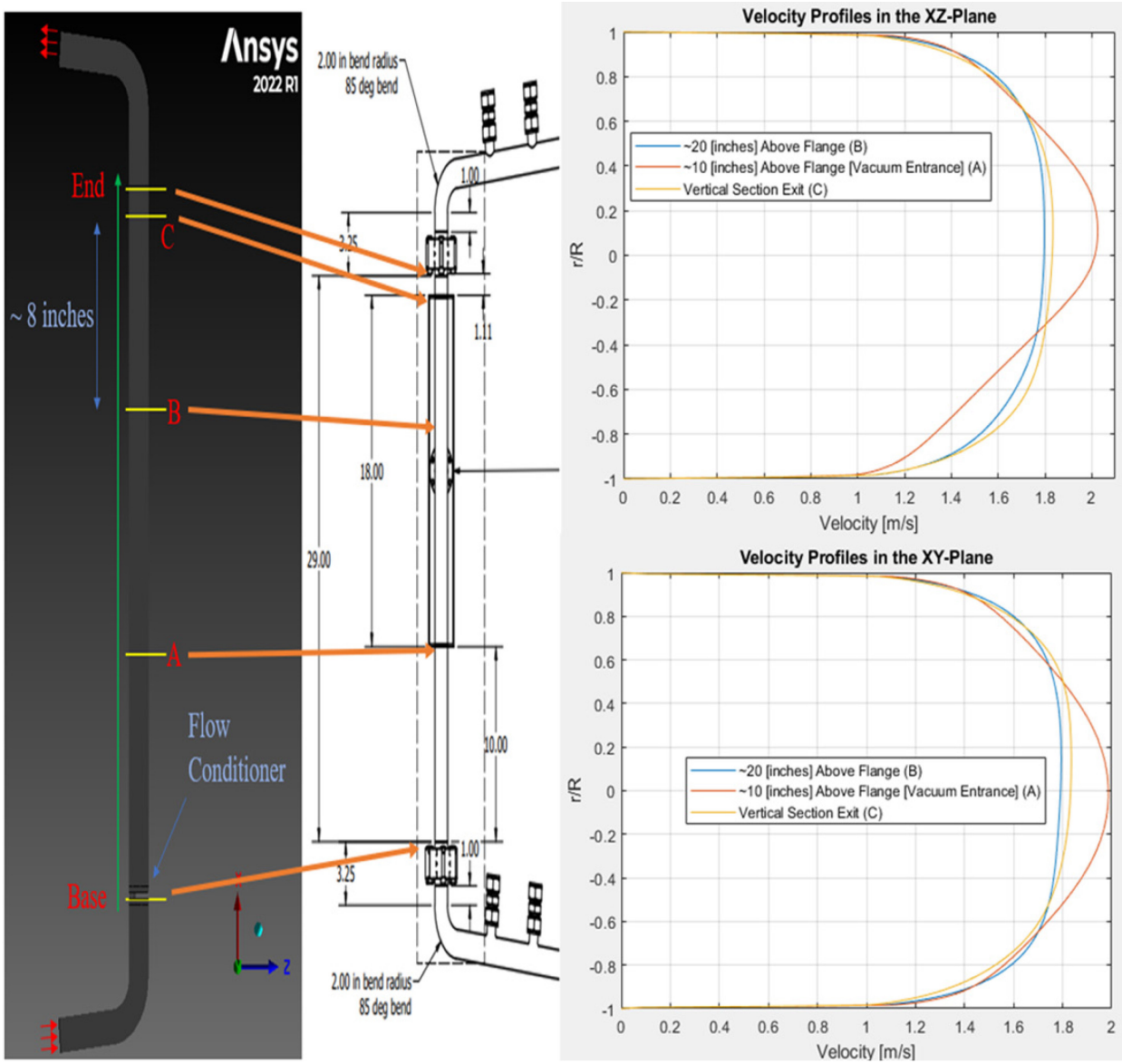

Figure 48. The location identification for the NEL design flow conditioner (left); velocity profiles in the XZ-Plane (top-right) and XY-Plane (bottom-right).

The results shown in Figure 47 and Figure 48 depict symmetric and near fully developed profile for the flow condioners. These results were taken from a realizable k-epsilon turbulence model with scalable wall treatment, see Appendix C for mesh metrics.

With the fine geometry of the flow conditioner and corrosive nature of molten salts a finite element model was evaluated to determine risk of failure, leading to debris travelling through the loop and potentially damaging the pump. This model was generated utilizing the pressure differential across the plate due to head losses. This pressure differential is a function of the geometry of the plate's face using the flow constriction equations outlined in Section 2.3.

While turbulent flow would introduce non-uniform pressures, this model displays the ability of the conditioner to handle the hydrostatic load the flow constriction creates. The peak stress in the flow conditioner is less than 0.1% the yield stress of 316 stainless steel as shown in Figure 49. The

introduction of turbulent flow is not expected to introduce stresses relevant to the yield strength of the material.

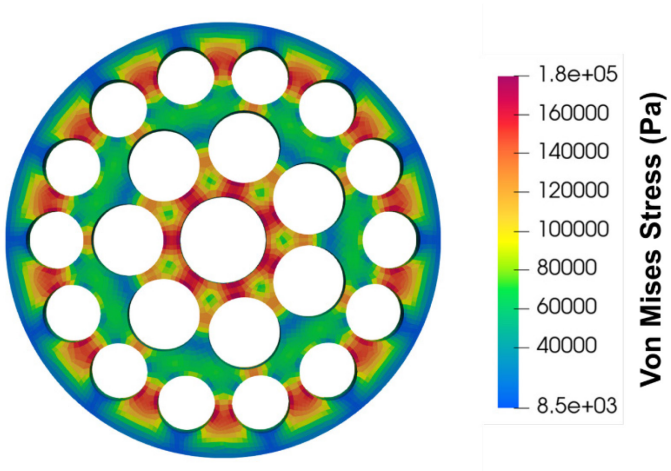

Figure 49. Laws flow conditioner geometry with finite element evaluation of stress.

4.5 CFD Future Work

Based on the obtained results, it is evident that achieving a fully developed flow profile at the entrance of the vacuum section is unattainable without mitigation or increasing the length scale which is not possible due to facility constraints. The implementation of additional components such as reducers and flow conditioners was investigated to enable a fully developed profile given the fixed length scale constraint. Certain geometries exhibited improvements, with some cases yielding an entirely developed flow profile. Remarkably, the incorporation of 0.5-in. reducers facilitated the attainment of profile development at the entrance with negligible differences in reducer type. The utilization of a flow conditioner demonstrated notable success in mitigating swirl-induced flow patterns while concurrently preserving operational capacity. However, both flow conditioners designs fell short of meeting the prerequisite for complete profile development prior to the vacuum section. The simulations of a NEL's type flow conditioner indicated that a nearly fully developed profile could be achieved if the length of the test section were reduced by 10 inches, thus rendering it 8 inches instead of the current 18 inches, immediately before entering the apparatus. Future work consists of analyzing the coupling of flow conditioners and reducers. By addition of the flow conditioner, the swirling effects can be corrected prior to entering the reducer thus allowing the flow to reach a fully developed profile near the analytical hydrodynamic length.

5. SUMMARY

The Molten Salt Tritium Transport Experiment (MSTTE) is a forced-convection fluoride salt loop with the capability to inject hydrogen isotopes into flowing molten salt and to measure transport phenomena such as permeation through metals and evolution from free-surfaces. MSTTE is designed to be versatile to test potential control technology in future campaigns. MSTTE is fabricated from mating a Copenhagen Atomics Pump Salt Loop with an external test section equipped with hydrogen injection and measurement capabilities. Custom designed and fabricated experiment components such as the hydrogen injection system, permeation test section, diagnostics, and gas distribution system were discussed in detail. System-level tritium transport modeling was developed using SAM to investigate experiment parameters such as hydrogen source terms, salt flow rate, and salt temperature. An increased source term affects the permeation rate through the test section as well as concentration in the loop. The transport is nominally limited by mass transfer in the salt phase. Thus, an increase in flow rate and temperature affects the transient time to reach a steady state, increasing both parameters and resulting in a shorter amount of time required to reach steady state. Future modeling work will investigate evolution in the plenum, tritium leakage through the non-test section loop piping, as well as tritium leakage, and heat loss through the test section outer vacuum shell wall. Computational fluid dynamics of the salt flow in the as-designed permeation test section showed that salt flow was not fully developed. The addition of flow conditioners and reducers is required to achieve fully developed flow. However, design and analysis of the conditioned test section is in the preliminary phase. Future design work includes establishing a fully developed flow design as well as implementing an in-vacuo IR heating system for the salt-contacting piping. These tasks will be addressed early in FY-24 and construction of MSTTE is anticipated to be completed in FY-24.

6. REFERENCES

1. Forsberg, C., *The advanced high-temperature reactor: High-temperature fuel, liquid salt coolant, liquid-metal-reactor plant.* Progress in Nuclear Energy, 2005. **47**(1): p. 32-43.
2. Serp, J., et al., *The molten salt reactor (MSR) in generation IV: Overview and perspectives.* Progress in Nuclear Energy, 2014. **77**: p. 308-319.
3. Ouyang, F.-Y., et al., *Effect of moisture on corrosion of Ni-based alloys in molten alkali fluoride FLiNaK salt environments.* Journal of Nuclear Materials, 2013. **437**(1): p. 201-207.
4. Raiman, S.S. and S. Lee, *Aggregation and data analysis of corrosion studies in molten chloride and fluoride salts.* Journal of Nuclear Materials, 2018. **511**: p. 523-535.
5. Sulejmanovic, D., et al., *Validating modern methods for impurity analysis in fluoride salts.* Journal of Nuclear Materials, 2021. **553**: p. 152972.
6. Forsberg, C.W., et al., *Tritium Control and Capture in Salt-Cooled Fission and Fusion Reactors: Status, Challenges, and Path Forward.* Nuclear Technology, 2017. **197**(2): p. 119-139.
7. *Implementation of Recommendations from the Tritium Studies Synthesis Report*. 2019, Canadian Nuclear Safety Commission.
8. *Doses in Our Daily Lives*. Radiation Protection April 26, 2022.
9. Wu, X., et al., *Evaluation of public dose from FHR tritium release with consideration of meteorological uncertainties.* Science of The Total Environment, 2020. **709**: p. 136085.
10. *Management of Waste Containing Tritium and Carbon-14*, in *Technical Reports Series No. 421*. 2004, IAEA: Vienna, Austria.
11. Stempien, J.D., *Tritium Transport, Corrosion, and Fuel Performance Modeling in the Fluoride Salt-Cooled High-Temperature Reactor (FHR)*, in *Department of Nuclear Science and Engineering*. 2015, Massachusetts Institute of Technology.
12. Briggs, R.B., *Distribution of Tritium in a 1000-MW(e) MSBR*. 1970, Oak Ridge National Laboratory.
13. Andrews, H.B., et al., *Review of molten salt reactor off-gas management considerations.* Nuclear Engineering and Design, 2021. **385**: p. 111529.
14. Chadwick, M.B., et al., *ENDF/B-VII. 1 nuclear data for science and technology: cross sections, covariances, fission product yields and decay data.* Nuclear data sheets, 2011. **112**(12): p. 2887-2996.
15. Humrickhouse, P.W. and T.F. Fuerst, *Tritium Transport Phenomena in Molten-Salt Reactors*. 2020: United States. INL/EXT-20-59927-Rev000
16. Fuerst, T.F., C.N. Taylor, and P.W. Humrickhouse, *Tritium Transport Phenomena in Molten-Salt Reactors: Molten Salt Tritium Transport Experiment Design*. 2021: United States. INL/EXT-21-63108-Rev000
17. Atomics, C. *Molten salt loop*. 2023; Available from: https://www.copenhagenatomics.com/products/molten-salt-loop/.
18. Andrews, H.B., J. McFarlane, and K.G. Myhre, *Monitoring noble gases (Xe and Kr) and aerosols (Cs and Rb) in a molten salt reactor surrogate off-gas stream using laser-induced breakdown spectroscopy (LIBS).* Applied Spectroscopy, 2022. **76**(8): p. 988-997.
19. Felmy, H.M., et al., *On-line monitoring of gas-phase molecular iodine using Raman and fluorescence spectroscopy paired with chemometric analysis.* Environmental Science & Technology, 2021. **55**(6): p. 3898-3908.
20. Vergari, L., M. Borrello, and R.O. Scarlat. *Electrochemical Sensors and Techniques for Redox Potential and Tritium Transport in a Neutron-Irradiated Molten Flibe Salt Loop*. in *Electrochemical Society Meeting Abstracts 242*. 2022. The Electrochemical Society, Inc.
21. Williams, A.N., G.G. Galbreth, and J. Sanders, *Accurate determination of density, surface tension, and vessel depth using a triple bubbler system.* Journal of industrial and engineering chemistry, 2018. **63**: p. 149-156.
22. Hu, R., et al., *SAM Theory Manual*. 2021, Argonne National Laboratory: Lemont, IL.

23. Lindsay, A.D., et al., *2.0 - MOOSE: Enabling massively parallel multiphysics simulation.* SoftwareX, 2022. **20**: p. 101202.
24. Mui, T., R. Hu, and Q. Zhou. *Integration of a tritium transport model in SAM for FHR modeling*. in *Transactions of the American Nuclear Socity*. 2023. Phoenix, AZ.
25. Atsumi, H., et al., *Desorption of hydrogen trapped in carbon and graphite.* Journal of Nuclear Materials, 2013. **442**: p. S746-S750.
26. Dolan, K.P., *Tritium Retention in Nuclear Graphite, System-Level Transport, and Management Strategies for the Fluoride-Salt-Cooled High-Temperature Reactor*. 2020, Massachusetts Institute of Technology.
27. Fukada, S. and A. Morisaki, *Hydrogen permeability through a mixed molten salt of LiF, NaF and KF (Flinak) as a heat-transfer fluid.* Journal of Nuclear Materials, 2006. **358**: p. 235-242.
28. Malinauskas, A.P. and D.M. Richardson, *The Solubilities of Hydrogen, Deuterium, and Helium in Molten Li2BeF4.* Industrial & Engineering Chemistry Fundamentals, 1974. **13**: p. 242-245.
29. Tanabe, T., et al., *Hydrogen Transport in Stainless Steels.* Journal of Nuclear Materials, 1984. **122-123**: p. 1568-1572.
30. Rader, J.D., M.S. Greenwood, and P.W. Humrickhouse, *Verification of Modelica-Based Models with Analytical Solutions for Tritium Diffusion.* Nuclear Technology, 2018. **203**: p. 58-65.

Appendix A

Numerical Model for Hydrogen Transport

The Hydrogen Injection System model was defined by a system of equations for mass flux through the system, assuming steady state conditions with equal flux through each boundary. The equations were iterated down the length injection system tubing, accounting for increasing concentration in the salt downstream. The system is defined by the following flux equations:

The mass flux through the gas-wall interface is defined as:

$$J_1 = k_d P_1 - k_r {C_{wg}}^2 \tag{A.1}$$

The mass flux through the pipe wall:

$$J_2 = \frac{2D_s(C_{wg} - C_{wl})}{D_o \ln\left(\frac{D_o}{D_i}\right)} \tag{A.2}$$

The mass flux through the wall-liquid interface:

$$J_3 = k_r {C_{wl}}^2 - k_d \frac{C_{lw}}{K_H} \tag{A.3}$$

The mass flux through the boundary layer of the salt:

$$J_4 = k_t(C_{lw} - C_B) \tag{A.4}$$

The system is defined by steady state mass flux, with:

$$J = J_1 = J_2 = J_3 = J_4 \tag{A.5}$$

Where:

k_d = Dissociation constant of hydrogen (mold m^{-2} s^{-1} $Pa^{-1)}$

k_r = Recombination constant of hydrogen (atoms m^3 $mols^{-1}$ s^{-1})

P_1 = Gas Pressure (Pa)

D_s = Diffusivity of hydrogen in salt (m^2 s^{-1})

D_o = Outer diameter of tube (m)

D_i = Inner diameter of tube (m)

K_H = Henry's law solubility of hydrogen in salt (mol m^{-3} Pa^{-1})

k_t = Mass Transfer coefficient (m s^{-1})

C_{wg} = Concentration of hydrogen in wall at gas interface (mol m^{-3})

C_{wl} = Concentration of hydrogen in wall at liquid interface (mol m^{-3})

C_{lw} = Concentration of hydrogen in liquid at wall interface (mol m^{-3})

C_B = Concentration of hydrogen in boundary layer (mol m^{-3})

The solution is defined by an initial condition of $C_B = 0$, with no hydrogen in the salt as it enters the injection system. All other concentrations as well as mass flux are unknown. Using equations A.1-A.4 and constant flux, a system of equations can be generated by $J_1 = J_2$, $J_2 = J_3, J_3 = J_4$, solving for C_{wg}, C_{wl}, C_{lw}. Flux can then be solved for using these concentrations.

The solution to this system is done iteratively through discretized sections down the length of the injection tube, starting at the entrance. As salt moves through the injection system and down the length of the tubes, the concentration of hydrogen increases. This alters the total flux through different sections of the tube.

The permeation through the section is defined by:

$$n_{perm} = J\,S \tag{A.6}$$

The total permeation up to this point:

$$\dot{n} = (C_B\,\dot{V}) + n_{perm} \tag{A.7}$$

The concentration in the salt after it passes the section:

$$C_{B(new)} = \dot{n}/\dot{V} \tag{A.8}$$

Where:

S = Surface area of the Section (m^2)

$\dot{V}$ = Volumetric flow rate (m^3 s^{-1})

This model utilized 50 segments. The concentration in the salt and total permeation of hydrogen through one pass of the injection system are defined by $C_{B(new)}$ and $\dot{n}$ as found through the final iterative section, respectively.

Appendix B

Code Compliance Calculations

ASME B31.3 outlines codes for design and manufacturing of Process Piping and Tubing, ensuring proper thickness and reinforcement to account for pressurization and corrosion of the system. For MSTTE, B31.3 defines the required thickness for straight wall and bends on the salt loop section, as well as the weld reinforcement area required for the branch connections for sensor ports. The loop uses 1.5-in. outer diameter tubing.

The minimum thickness for straight sections was calculated, as well the inside (intrados) and outside (extrados) thickness required on bends (Table B-1). The results (Table B-2) values include a 0.5-mm allowance for corrosion of the system in addition to the thickness required for strength under pressurized conditions.

Table B-1. Straight pipe and bend equations and parameters.

Parameter	Equation/Symbol	Value
Temperature	T	700°C
Pressure	P	0.3 MPa
Diameter	D	38.1 mm (1.5 in.)
Stress Value	S	29.6 MPa
Quality Factor	E	0.8
Weld Joint Reduction Factor	W	0.68
Thin Wall Temperature Coefficient	Y	0.7
Straight Pipe Thickness	$t = \frac{PD}{2(SEW + PY)}$	
Pipe Bend Radius (Center)	R	50.8 mm (2 in.)
Bend Radius Coefficient (Intrados)	$I = \frac{(4R/D) - 1}{(4R/D) - 2}$	1.3
Bend Radius Coefficient (Intrados)	$I = \frac{(4R/D) + 1}{(4R/D) + 2}$	0.86
Bend Pipe Thickness	$t = \frac{PD}{2[(SEW/I) + PY]}$	
Corrosion Allowance	c	0.5 mm
Minimum Required Thickness	$t_m = t + c$	

Table B-2. Pipe thickness.

Minimum Required Pipe Wall Thickness		
	Thickness (in)	Thickness (mm)
Straight Pipe	0.034	0.85
Bend (Intrados)	0.038	0.95
Bend (Extrados)	0.032	0.80

Additional reinforcement at welds for ports and the injection system is necessary to ensure strength under pressure and corrosion factors at the tee made by the inclusion of the ports. This area is accounted for by a combination excess thickness of the pipe wall and external weld reinforcement. A_1 defines the required reinforcement, while A_2 and A_3 define excess thickness of the pipe and port walls. Where excess

thickness is insufficient, external reinforcement is necessary and denoted by A_4 in the following diagram, which includes the thickness of the weld. The equations are reported in Table B3 and results reported in Table B4.

Table B-3. Branch reinforcement equations.

Parameter	Equation/Symbol
Required Reinforcement	$A_1 = t_h d_1(2 - sin\beta)$
Pipe Wall Excess Thickness	$A_2 = (2d_2 - d_1)(T_h - t_h - c)$
Branch Excess Thickness	$A_3 = 2L_4(T_b - t_b - c)/sin\beta$
Minimum Additional Reinforcement	$A_4 = A_1 - A_2 - A_3$

Table B-4. Branch reinforcement requirements.

Required Branch Reinforcement			
	Required Reinforcement (in^2)	Excess Sidewall Area (in^2)	Additional Reinforcement Required (in^2)
Injection System - Salt Flow	0.064	0.171	-0.107
Injection System - Permeator Ports	0.011	0.033	-0.022
Lower Leg Sensor Ports	0.028	0.020	0.009

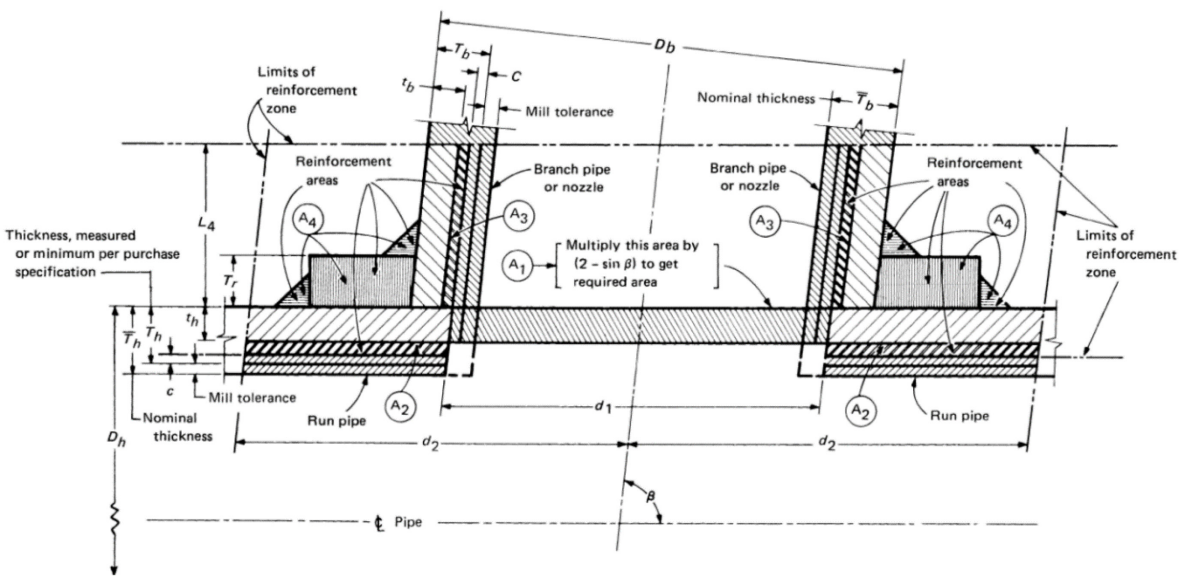

Figure B-1. Geometry definitions for Table B-3.

The injection system includes redundant sidewall thickness to where external reinforcement is not needed. The sensor ports, however, have a small requirement of additional reinforcement required, but will be sufficiently covered by a standard 0.25-in. fillet weld.

Appendix C

Additional Information on CFD Analysis

Table C-1. Mesh information and metrics.

Case	Nodes	Cells
Laminar	3,153,510	3,105,200
Turbulent	3,153,510	3,105,200
Concentric 1 in.	2,831,543	2,773,125
Concentric 0.5 in.	6,009,462	5,905,750
Eccentric 1 in.	3,211,616	3,154,275
Eccentric 0.5 in.	1,299,136	1,270,215
Reverse Eccentric 1 in.	1,905,336	1,865,250
Reverse Eccentric 0.5 in.	2,576,224	2,519,740
Flow Condition Law Design	9,793,040	9,452,796
Flow Condition NEL Design	9,660,896	9,361,312

A36	85 °
A43	85 °
H37	4 in
H45	4 in
L53	2 in
R35	2 in
R55	2 in
V48	3.25 in
V49	10 in
V50	18 in
V51	1.11 in
V52	3.25 in

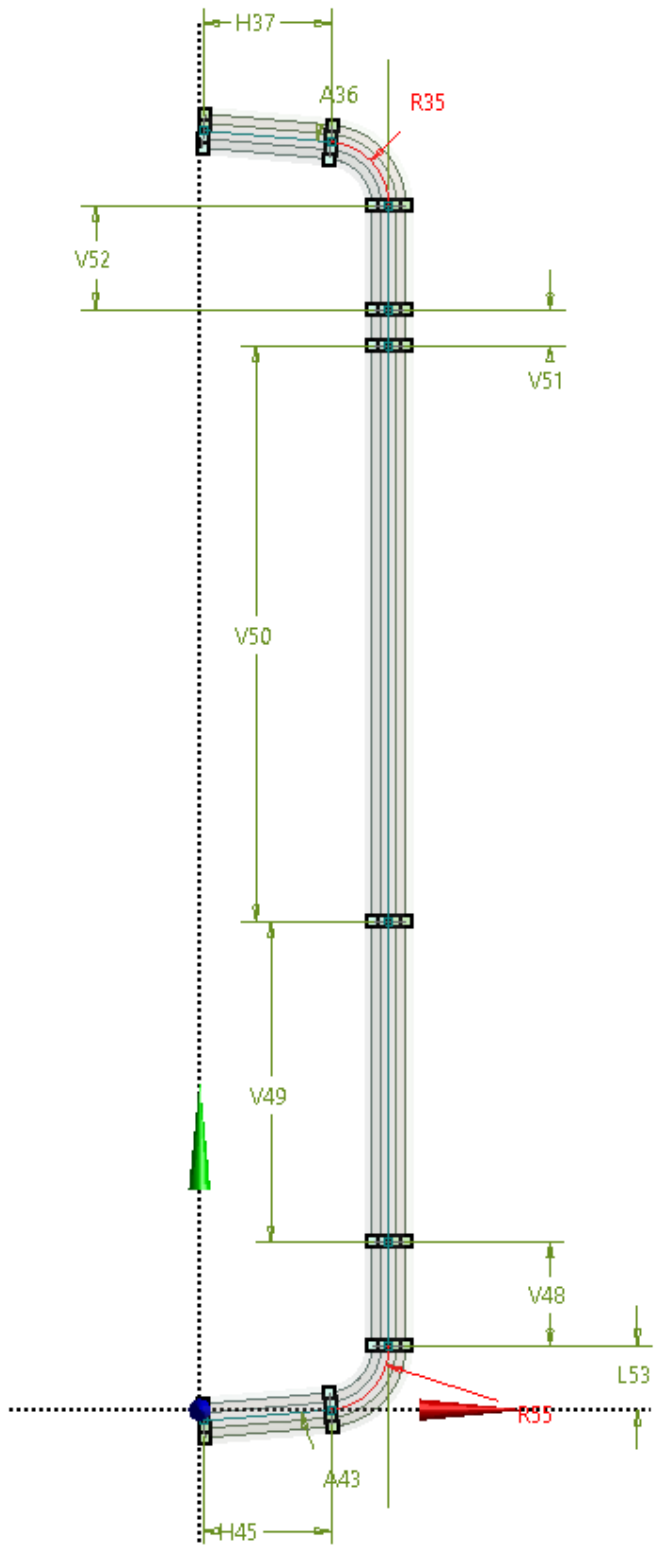

Figure C-1. MSTTE Permeator ANSYS geometry with dimensions.